RESEARCH ARTICLE

Key Points:
- Pressure-scrambling terms were decomposed into several contributions
- Turbulence-turbulence and buoyancy components of pressure-scrambling terms are most significant
- A simple linear model for pressure-scrambling terms performs reasonably well

Correspondence to:
R. Heinze,
rieke.heinze@mpimet.mpg.de

Analysis of pressure-strain and pressure gradient-scalar covariances in cloud-topped boundary layers: A large-eddy simulation study

Rieke Heinze[1,2], Dmitrii Mironov[3], and Siegfried Raasch[1]

[1]Institut für Meteorologie und Klimatologie, Leibniz Universität Hannover, Hannover, Germany, [2]Max Planck Institut, Atmosphäre im Erdsystem, Hamburg, Germany, [3]Deutscher Wetterdienst, Forschung und Entwicklung, FE14, Offenbach, Germany

Abstract A detailed analysis of the pressure-scrambling terms (i.e., the pressure-strain and pressure gradient-scalar covariances) in the Reynolds-stress and scalar-flux budgets for cloud-topped boundary layers (CTBLs) is performed using high-resolution large-eddy simulation (LES). Two CTBLs are simulated — one with trade wind shallow cumuli, and the other with nocturnal marine stratocumuli. The pressure-scrambling terms are decomposed into contributions due to turbulence-turbulence interactions, mean velocity shear, buoyancy, and Coriolis effects. Commonly used models of these contributions, including a simple linear model most often used in geophysical applications and a more sophisticated two-component-limit (TCL) nonlinear model, are tested against the LES data. The decomposition of the pressure-scrambling terms shows that the turbulence-turbulence and buoyancy contributions are most significant for cloud-topped boundary layers. The Coriolis contribution is negligible. The shear contribution is generally of minor importance inside the cloudy layers, but it is the leading-order contribution near the surface. A comparison of models of the pressure-scrambling terms with the LES data suggests that the more complex TCL model is superior to the simple linear model only for a few contributions. The linear model is able to reproduce the principal features of the pressure-scrambling terms reasonably well. It can be applied in the second-order turbulence modeling of cloud-topped boundary layer flows, provided some uncertainties are tolerated.

1. Introduction

Modeling the pressure-scrambling terms, i.e., the pressure-strain and pressure gradient-scalar covariances in the Reynolds-stress and scalar-flux budgets, respectively, is one of the major challenges in second-order turbulence modeling for numerical weather prediction and climate model applications [e.g., *Miles et al.*, 2004; *Mironov*, 2001, 2009]. The terms are of fundamental importance in the Reynolds-stress and scalar-flux budgets as shown by e.g., *Lenschow et al.* [1980], *Mironov et al.* [2000], and *Heinze et al.* [2015]. In the Reynolds-stress budget, for example, the pressure terms act to redistribute the kinetic energy produced by shear and/or buoyancy between the velocity-variance components, thus reducing the turbulence anisotropy generated by shear, buoyancy, and rotation.

Moeng and Wyngaard [1986]; *Andrén and Moeng* [1993]; *Mironov* [2001]; and *Miles et al.* [2004] used large-eddy simulations (LES) to analyze the pressure-scrambling terms in dry convective and neutral atmospheric boundary-layer flows. The present study extends previous work by considering the atmospheric boundary-layer flows capped by shallow clouds. We use very high-resolution LES of a cumulus-topped and a stratocumulus-topped boundary layer (i) to analyze the vertical structure of the pressure-scrambling terms in the Reynolds-stress and the scalar-flux budgets, and (ii) to test the applicability of some commonly used parameterizations (models) of the pressure-scrambling terms to the boundary layers capped by shallow clouds. (Note that the terms "parameterization" and "model" are used interchangeably in this context. The term "parameterization" seems to be more popular in numerical weather prediction and climate modeling community.) *Heinze et al.* [2015, hereinafter H15] analyzed the second-moment budgets in cloud-topped boundary-layer flows generated with LES and demonstrated that the pressure-scrambling terms are of paramount importance in maintaining the Reynolds-stress and the scalar-flux budgets. A step forward is made in the present paper, where a detailed analysis of the pressure-scrambling terms is performed.

The pressure-strain and pressure gradient-scalar covariances are usually decomposed into contributions due to nonlinear turbulence-turbulence interactions, mean velocity shear, buoyancy, and Coriolis effects [e.g., *Launder et al.*, 1975; *Lumley*, 1978; *Zeman*, 1981; *Pope*, 2000, p. 390]. The treatment is based on a respective decomposition of the turbulent pressure field and the solution of the Poisson equations for the above contributions to the fluctuating pressure field. The contributions to the pressure-scrambling terms are then modeled (parameterized) separately.

The first parameterization of the pressure-strain covariance was proposed by *Rotta* [1951]. Some modelers applied the Rotta return-to-isotropy parameterization to the entire pressure-term. Others, as e.g., *Launder et al.* [1975], model only the so-called slow turbulence-turbulence contribution with the Rotta return-to-isotropy parameterization. The so-called rapid contributions, which are the contributions due to mean shear, buoyancy, and Coriolis effects, are modeled separately by setting them proportional to the mean-shear, buoyancy, and Coriolis production/destruction terms in the Reynolds-stress budgets. In a similar fashion, the slow turbulence-turbulence contribution to the pressure gradient-scalar covariance is modeled with the Rotta-type relaxation parameterization, whereas the rapid contributions are taken to be proportional to the mean-shear, buoyancy, and Coriolis terms in the scalar-flux budget. These parameterizations for the rapid contributions are linear in the second-order moments. The Rotta-type return-to-isotropy parameterization for the slow contributions and the linear parameterizations for the rapid contributions form what we refer to as "the basic model" for the pressure-scrambling terms in the Reynolds-stress and scalar-flux budgets. This basic model is most often used in geophysical applications [see e.g., *Zeman*, 1981; *Umlauf and Burchard*, 2005].

In addition to the linear models (parameterizations), numerous more elaborate nonlinear models for the pressure-scrambling terms exist [e.g., *Lumley*, 1978; *Ristorcelli et al.*, 1995; *Craft et al.*, 1996]. Usually, the nonlinear models perform better than linear models, especially in flows with large departure from isotropy (like boundary-layer flows affected by buoyancy and/or rotation). However, they usually consist of rather complex expressions which are computationally too expensive for routine geophysical applications where turbulence is one of many physical processes to model [*Andrén and Moeng*, 1993; *Mironov*, 2009].

Turbulence measurements or results of turbulence-resolving models, such as LES and DNS (direct numerical simulations), are used to develop and test turbulence closure models and to determine (disposable) model constants. Direct measurements of pressure-strain and pressure gradient-scalar covariances in the atmospheric boundary layer are rather difficult since the atmospheric pressure fluctuations are very small in comparison to the mean pressure. Pressure probes tend to disturb the pressure field, leading to distorted measurements [*Wilczak*, 1984; *Wilczak and Bedard*, 2004]. In early studies, the pressure-scrambling terms were determined indirectly as residuals of second-moment budgets [e.g., *Wyngaard and Coté*, 1971; *Lenschow et al.*, 1980]. This approach is problematic as the residuals might also include accumulated measurement errors which can be quite large [*Stull*, 1988, p. 163]. The first direct measurement of the horizontal pressure gradient-temperature covariance in the atmospheric surface layer was conducted by *Wilczak and Bedard* [2004] by means of a pressure-probe based on *Nishiyama and Bedard* [1991]. *Nguyen et al.* [2013] were the first to present measurements of numerous pressure-scrambling terms in the surface layer (including four components of the pressure-strain covariance tensor and two components of the pressure gradient-temperature covariance vector). Detailed insight into the vertical structure of the pressure-scrambling terms and their contributions in the entire boundary layer is gained from LES studies. *Moeng and Wyngaard* [1986] and *Mironov* [2001] tested parameterizations of pressure gradient-scalar covariances in the dry convective boundary layer, and *Andrén and Moeng* [1993] concentrated on the pressure-scrambling terms in the neutral boundary layer. It should be noted that detailed analysis of the pressure-scrambling terms can only be performed on the basis of numerical data from LES or from DNS. Apart from the fact that in situ measurements of fluctuating pressure are rather difficult [*Wilczak and Bedard*, 2004], the decomposition of the fluctuating pressure is simply impossible on the basis of observational data.

In the present work, we use high-resolution LES of H15 to decompose the fluctuating pressure and to determine all contributions to the pressure-scrambling terms in the Reynolds-stress and scalar-flux budgets. A simple linear model and a more sophisticated two-component-limit (TCL) nonlinear model are then compared to LES data and the model constants are estimated.

In what follows, a standard notation is used where t is time, $x_i = (x_1, x_2, x_3)$ are the Cartesian coordinates, g is the acceleration due to gravity, f is the Coriolis parameter, L_v is the latent heat of evaporation, c_p is the specific heat at constant pressure, R_v and R_d are the gas constants for water vapor and for dry air, respectively, $u_i = (u_1, u_2, u_3)$ are the velocity components, p is the perturbation pressure (deviation of pressure from the hydrostatically and geostrophically balanced pressure), T is the absolute temperature, θ is the potential temperature, q_v is the (water vapor) specific humidity, and q_l is the liquid water specific humidity. Reference values of potential temperature and density are denoted by θ_0 and ρ_0, respectively. The virtual potential temperature is defined as $\theta_v = \theta\{1 + [(R_v/R_d) - 1]q_v - q_l\}$. A generic variable s denotes a quasi-conservative scalar that is either the liquid water potential temperature $\theta_l = \theta - (\theta/T)(L_v/c_p)q_l$ or the total water specific humidity $q_t = q_v + q_l$. The Einstein summation convention for repeated indices is used. The Kronecker delta is denoted by δ_{ij}, and the Levi-Civita tensor is denoted by ε_{ijk}. An overbar $\overline{()}$ denotes a resolved-scale (filtered) variable carried by the large-eddy model, and a single prime $()'$ indicates a deviation from the filtered quantity (i.e., a subfilter-scale fluctuation). In section 2.2 and Appendix A, where a decomposition of the fluctuating pressure is explained, the angle brackets $\langle () \rangle$ denote a horizontal mean, and a double prime $()''$ denotes a deviation therefrom. In the rest of the paper, the angle brackets denote the quantities obtained from LES data by means of averaging over horizontal planes and over time.

The paper is organized as follows. Section 2.1 provides a brief description of the large-eddy model used and of the simulated cases. The decomposition of the turbulent pressure is explained in section 2.2. Section 3 presents results from the analysis of LES data. First (section 3.1), the components of the turbulent pressure are discussed. Then, vertical profiles of various contributions to the pressure-strain covariances (section 3.2) and to the pressure gradient-scalar covariances (section 3.3) are presented and analyzed. In section 3.4, some commonly used models (parameterizations) of the turbulence-turbulence (section 3.4.1), the buoyancy (section 3.4.2), and the mean velocity shear (section 3.4.3) contributions to the pressure-strain and pressure gradient-scalar covariances are tested against the LES data, and the model constants are estimated. Summary and conclusions are presented in section 4.

2. Large-Eddy Simulations

2.1. Large-Eddy Model and Simulated Cases
In this study, the parallelized large-eddy model PALM [*Raasch and Schröter*, 2001; *Maronga et al.*, 2015] is utilized. Two cloud-topped boundary layers (CTBLs), the shallow trade wind cumulus case BOMEX [*Siebesma et al.*, 2003], and the nocturnal stratocumulus case DYCOMS-II, RF01 [*Stevens et al.*, 2005] (hereinafter referred to as simply DYCOMS), are simulated with a fine grid spacing of 5 m in all spatial directions.

The simulation setup and the model configuration used are exactly the same as described in H15. Further details of the LES model PALM and of the simulation setup are given in H15 and the references therein. The turbulence statistics discussed below are the result of averaging the LES fields horizontally and over the last 3 h of the simulation in the BOMEX case and over the last 2 h of simulations in the DYCOMS case. The number of samples is 540 for BOMEX and 360 for DYCOMS.

2.2. Decomposition of Pressure Covariances
In second-order turbulence modeling, the standard approach to treat the pressure-scrambling terms is to decompose them into contributions due to nonlinear turbulence-turbulence interactions (T), mean velocity shear (S), buoyancy (B), and the Coriolis effects (C) and to model these contributions separately [e.g., *Zeman*, 1981]. Applying this decomposition to the resolved-scale part of the pressure-strain covariance defined as

$$\Pi_{ij} = \frac{1}{\rho_0}\left\langle \bar{p}''\left(\frac{\partial \bar{u}_i''}{\partial x_j} + \frac{\partial \bar{u}_j''}{\partial x_i}\right)\right\rangle, \tag{1}$$

and to the pressure gradient-scalar covariance defined as

$$\Pi_{si} = -\frac{1}{\rho_0}\left\langle \bar{s}''\frac{\partial \bar{p}''}{\partial x_i}\right\rangle, \tag{2}$$

yields

$$\Pi_{ij} = \Pi_{ij}^{T} + \Pi_{ij}^{S} + \Pi_{ij}^{B} + \Pi_{ij}^{C} + \Pi_{ij}^{SG} + \Pi_{ij}^{SU}, \tag{3}$$

$$\Pi_{si} = \Pi_{si}^{T} + \Pi_{si}^{S} + \Pi_{si}^{B} + \Pi_{si}^{C} + \Pi_{si}^{SG} + \Pi_{si}^{SU}, \tag{4}$$

Notice that, as different from the ensemble-mean modeling framework, an additional contribution due to the subgrid scale (SGS) Reynolds stress and SGS scalar flux (superscript SG) should be considered in the LES [see *Mironov*, 2001, for details]. Further contributions result due to the prescribed large-scale subsidence (SU) in both CTBLs (see Appendix A in H15 for details).

The components of Π_{ij} and Π_{si} are determined by using the corresponding contributions to the fluctuating pressure,

$$\bar{p}'' = \bar{p}_{T}'' + \bar{p}_{S}'' + \bar{p}_{B}'' + \bar{p}_{C}'' + \bar{p}_{SG}'' + \bar{p}_{SU}'', \tag{5}$$

which in turn are determined from the following set of Poisson equations:

$$\frac{1}{\rho_0} \frac{\partial^2 \bar{p}_T''}{\partial x_i^2} = -\frac{\partial^2}{\partial x_i \partial x_j} \left(\bar{u}_i'' \bar{u}_j'' - \langle \bar{u}_i'' \bar{u}_j'' \rangle \right), \tag{6}$$

$$\frac{1}{\rho_0} \frac{\partial^2 \bar{p}_S''}{\partial x_i^2} = -2 \frac{\partial \bar{u}_j''}{\partial x_i} \frac{\partial \langle \bar{u}_i \rangle}{\partial x_j}, \tag{7}$$

$$\frac{1}{\rho_0} \frac{\partial^2 \bar{p}_B''}{\partial x_i^2} = \frac{g}{\theta_0} \frac{\partial \bar{\theta}_v''}{\partial x_3}, \tag{8}$$

$$\frac{1}{\rho_0} \frac{\partial^2 \bar{p}_C''}{\partial x_i^2} = -\varepsilon_{ijk} f_j \frac{\partial \bar{u}_k''}{\partial x_i}, \tag{9}$$

$$\frac{1}{\rho_0} \frac{\partial^2 \bar{p}_{SG}''}{\partial x_i^2} = -\frac{\partial^2 \tau_{ij}''}{\partial x_i \partial x_j}, \tag{10}$$

$$\frac{1}{\rho_0} \frac{\partial^2 \bar{p}_{SU}''}{\partial x_i^2} = -w_{\text{subs}} \left(\frac{\partial^2 \bar{u}_1''}{\partial x_1 \partial x_3} + \frac{\partial^2 \bar{u}_2''}{\partial x_2 \partial x_3} \right). \tag{11}$$

Here, $\tau_{ij} = \overline{u_i' u_j'}$ will be referred to, although somewhat loosely, as "the SGS Reynolds stress" which is computed by the PALM SGS model. (Note that, strictly speaking, the stress tensor is defined as $-\rho \tau_{ij}$, where ρ denotes the fluid density [see e.g., *Pope*, 2000, p. 581].) These Poisson equations are derived by taking the divergence of the LES momentum equation, subtracting from the resulting equation its horizontal mean (in order to obtain the equation for the deviation of pressure from its horizontal mean, $\bar{p}''$), and considering the various processes, contributing to the fluctuating pressure, separately.

To solve the Poisson equations (6)–(11), appropriate boundary conditions for the fluctuating pressure components at the surface and at the top of the model domain are needed which depend on the boundary conditions used for the momentum equations in the LES model. According to *Moeng and Wyngaard* [1986] and *Hadfield et al*. [1988], physically consistent boundary conditions can be derived by taking the vertical momentum equation at the surface. By applying the surface no-slip conditions for the velocity components ($\bar{u}_1 = \bar{u}_2 = \bar{u}_3 = 0$ at $x_3 = 0$) to the vertical momentum equation, we end up with

$$\frac{1}{\rho_0} \frac{\partial \bar{p}''}{\partial x_3} = \frac{g}{\theta_0} \bar{\theta}_v'' - \frac{\partial \tau_{3i}''}{\partial x_i} \quad \text{at} \quad x_3 = 0. \tag{12}$$

The surface boundary condition for the buoyancy and the SGS contributions should thus be $\frac{1}{\rho_0} \frac{\partial \bar{p}_B''}{\partial x_3}\big|_{x_3=0} = \frac{g}{\theta_0} \bar{\theta}_v''$ and $\frac{1}{\rho_0} \frac{\partial \bar{p}_{SG}''}{\partial x_3}\big|_{x_3=0} = -\frac{\partial \tau_{3i}''}{\partial x_i}$, respectively. For all the other fluctuating pressure components, a zero-gradient boundary condition holds. At the top of the model domain, the Neumann conditions in the form of a zero-gradient should be used.

The previous paragraph describes the pressure boundary conditions that should be used to be fully consistent with the momentum equations. However, a zero-gradient surface boundary condition is actually applied for the buoyancy and SGS pressure components due to numerical constraints which are further described

in Appendix A. Although the surface virtual potential temperature fluctuations are not negligible when prescribing horizontally homogeneous surface fluxes, we argue based on *Hadfield et al.* [1988] that surface temperature fluctuations in a convective boundary layer will have no major direct effect on the pressure field. The implemented pressure decomposition was validated by means of a simulation of a free convective boundary layer (simulation FC of H15). The components of the root-mean-square (r.m.s.) fluctuating pressure are in excellent agreement with results shown by *Moeng and Wyngaard* [1986]; *Mironov* [2001]; and *Miles et al.* [2004] (not shown). We argue that despite the choice of inconsistent surface pressure boundary conditions for the buoyancy and SGS components, physically meaningful results are obtained, and the core of the boundary layer, which is the center of our interest, will not be adversely affected.

There are principally two ways to calculate the fluctuating pressure. Three-dimensional LES fields of the velocity components and the virtual potential temperature can be used to solve the diagnostic Poisson equations (6)–(11) offline which was done, for example, by *Moeng and Wyngaard* [1986]; *Andrén and Moeng* [1993]; and *Mironov* [2001]. An online approach can also be chosen, where the fluctuating pressure components are determined during the simulation. This second option was chosen in the present study and further details about its implementation in the LES model PALM can be found in Appendix A.

A short comment on the decomposition of the pressure-velocity covariance appearing in the Reynolds-stress budget is in order. It is the pressure gradient-velocity covariance,

$$\Phi_{ij} = -\frac{1}{\rho_0} \left(\left\langle \bar{u}_i'' \frac{\partial \bar{p}''}{\partial x_j} \right\rangle + \left\langle \bar{u}_j'' \frac{\partial \bar{p}''}{\partial x_i} \right\rangle \right), \tag{13}$$

that enters the resolved Reynolds-stress equation [see e.g., *Stull*, 1988, p. 135]. This covariance is usually decomposed to separate out a trace-free part of Φ_{ij} [*Pope*, 2000, p. 388]. In the present study, the following decomposition of Φ_{ij} into pressure diffusion (transport), $\mathcal{T}_{ij}^{\mathrm{p}}$, and pressure–strain, Π_{ij}, is used:

$$\Phi_{ij} = \underbrace{-\frac{1}{\rho_0}\frac{\partial}{\partial x_k}\left(\delta_{jk}\langle \bar{u}_i''\bar{p}''\rangle + \delta_{ik}\langle \bar{u}_j''\bar{p}''\rangle\right)}_{\mathcal{T}_{ij}^{\mathrm{p}}} + \underbrace{\frac{1}{\rho_0}\left\langle \bar{p}''\left(\frac{\partial \bar{u}_i''}{\partial x_j} + \frac{\partial \bar{u}_j''}{\partial x_i}\right)\right\rangle}_{\Pi_{ij}}. \tag{14}$$

This decomposition is not unique. For example, a decomposition of Φ_{ij} into isotropic (diffusion) and deviatoric (trace-free) parts has also been advocated. It is still under debate which decomposition should generally be used in turbulence closures [e.g., *Lumley*, 1975; *Speziale*, 1985; *Groth*, 1991].

As pointed out in H15, the resolved and the subgrid scale contributions of the Reynolds-stress and scalar-flux budget terms should be taken into account to close the LES-based budgets to a good order. The sum of resolved and subgrid scale parts can then be interpreted as an approximation to the ensemble-mean quantities. H15 showed that even in very high-resolution LES the subgrid scale contributions to the pressure-strain covariance,

$$\mathcal{P}_{ij} = \frac{1}{\rho_0}\left\langle \overline{p'\left(\frac{\partial u_i'}{\partial x_j} + \frac{\partial u_j'}{\partial x_i}\right)}\right\rangle, \tag{15}$$

and to the pressure gradient-scalar covariance,

$$\mathcal{P}_{si} = -\frac{1}{\rho_0}\left\langle \overline{s'\frac{\partial p'}{\partial x_i}}\right\rangle, \tag{16}$$

remain nonnegligible, especially close to the surface. Hence, they should also be accounted for in the present study to obtain the best possible approximation of the ensemble-mean pressure-scrambling terms. The question remains, however, as to which contribution to the pressure-scrambling terms the SGS terms $\mathcal{P}_{ij}$ and $\mathcal{P}_{si}$ should be added. Following *Mironov* [2001], the SGS pressure terms given by (15) and (16) are attributed to the turbulence-turbulence contributions to the pressure-scrambling terms in the Reynolds-stress and scalar-flux budgets, respectively.
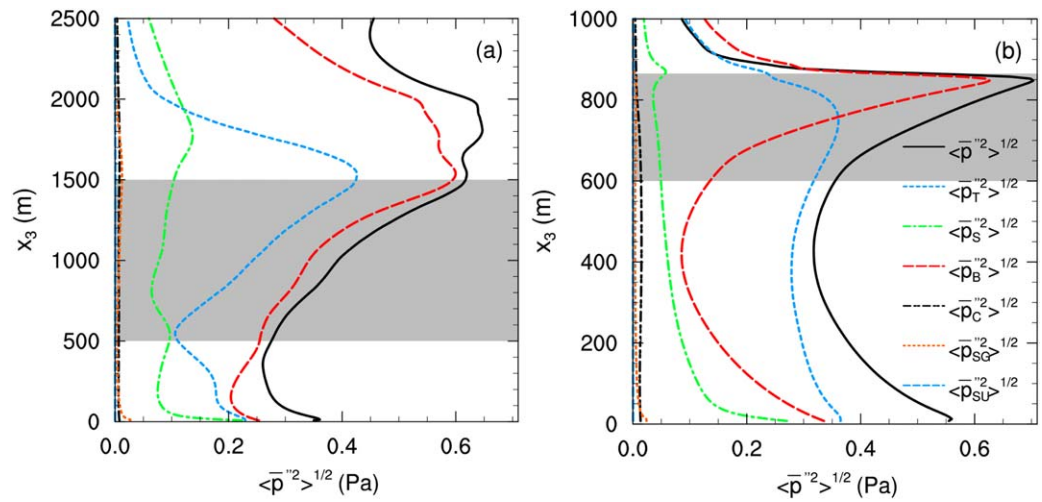
Figure 1. Vertical profiles of the components of the root-mean-square (r.m.s.) fluctuating pressure and the total r.m.s. pressure $\langle \bar{p}''^2 \rangle^{1/2}$ directly from the LES model for BOMEX (a) and DYCOMS (b). The profiles are obtained by means of averaging over the last 3 h of simulation for BOMEX and over the last 2 h of simulation for DYCOMS. The gray shading indicates the cloud layer.

3. Results

3.1. Contributions to Turbulent Pressure

Vertical profiles of the contributions to the root-mean-square (r.m.s.) fluctuating pressure of both CTBLs are shown in Figure 1. In the cumulus-topped boundary layer, Figure 1a, the buoyancy contribution is the largest over the entire boundary layer. The contribution due to turbulence-turbulence interactions is the second largest. Both, $\langle \bar{p}_T''^2 \rangle^{1/2}$ and $\langle \bar{p}_B''^2 \rangle^{1/2}$, exhibit a maximum at the top of the conditionally unstable layer ($x_3 \approx 1500$ m). The contribution due to mean shear is smaller but not negligible. It is at maximum near the surface where the velocity gradient is large. The turbulence-turbulence component is the largest component over most of the stratocumulus-topped boundary layer, Figure 1b. At the top of the stratocumulus layer, the buoyancy component becomes more important and dominates the total r.m.s. fluctuating pressure. As is the case for BOMEX, the contribution due to mean shear is less important than the contributions due to buoyancy and turbulence-turbulence interactions. In both CTBLs, the SGS contribution is fairly small. This is also the case for the Coriolis and large-scale subsidence components. The Coriolis and the large-scale subsidence components are not discussed in the following.

It should be pointed out that the square root of the sum of the six pressure variances shown in Figure 2 differs slightly from the square root of the total pressure variance. This indicates that the cross correlations of the pressure contributions are rather small. Thus, the pressure components are weakly correlated.

An important difference between the cumulus-topped and the stratocumulus-topped boundary layers is the relative importance of the buoyancy and the turbulence-turbulence contributions. The buoyancy contribution is the dominant one over the entire boundary layer for the cumulus case. In the stratocumulus case, the buoyancy contribution dominates only at the upper part of the cloud layer.

3.2. Contributions to Pressure-Strain Covariances

Vertical profiles of the diagonal elements Π_{11} and Π_{33} of the pressure-strain covariance tensor Π_{ij} are shown in Figure 3. The diagonal elements appear in the budget equations of the velocity variances. The principal role of the pressure-strain covariances is to return turbulence to an isotropic state by distributing TKE evenly between its components. This explains the sign of Π_{33} and Π_{11} in Figure 3: Π_{33} is mainly a loss-term (negative) and Π_{11} is a gain-term (positive) in the budget equations of the vertical and horizontal velocity variances, respectively, in both CTBLs. The horizontal-velocity variance grows at the expense of the vertical-velocity variance which is produced by buoyancy.

The contributions Π_{11}^B and Π_{33}^B due to buoyancy and Π_{11}^T and Π_{33}^T due to turbulence-turbulence interactions are of the same order of magnitude in the BOMEX case (Figures 3a and 3c). These are the leading contributions to the total pressure-strain covariance. The mean velocity shear contributions Π_{11}^S and Π_{33}^S are
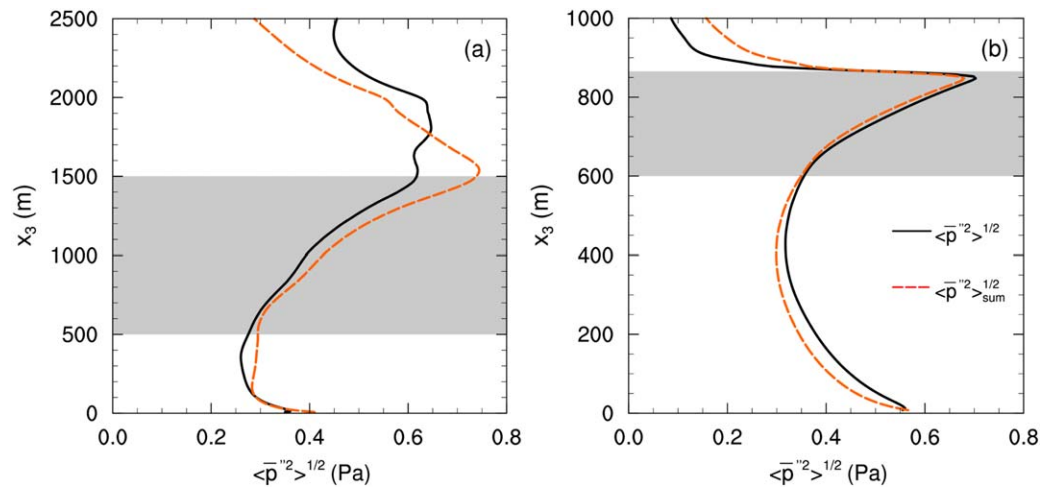
Figure 2. Vertical profiles of the total r.m.s. pressure $\langle \bar{p}''^2 \rangle^{1/2}$ directly from the LES model and the square root of the sum of the six pressure variances, $\langle \bar{p}''^2 \rangle_{sum}^{1/2} = \langle \bar{p}_T''^2 + \bar{p}_S''^2 + \bar{p}_B''^2 + \bar{p}_C''^2 + \bar{p}_{SG}''^2 + \bar{p}_{SU}'' + \rangle^{1/2}$ for BOMEX (a) and DYCOMS (b). Gray shading and time averaging as in Figure 1.

significant close to the surface and at the top of the subcloud mixed layer ($z \approx 500$ m). In the latter region, the wind turns quickly toward the geostrophic wind producing directional shear. In the DYCOMS case (Figures 3b and 3d), the turbulence-turbulence and buoyancy contributions to Π_{11} and Π_{33} are of similar importance apart from the upper part of the stratocumulus layer where the buoyancy contributions Π_{11}^B and Π_{33}^B dominate. There, the buoyancy production of the vertical-velocity variance is very large (cf. H15, Figure 5f). In DYCOMS, the shear contributions Π_{11}^S and Π_{33}^S are of minor importance over most of the boundary layer. Close to the surface, the shear contributions are of the same order of magnitude as the buoyancy and turbulence-turbulence contributions. The SGS contributions Π_{11}^{SG} and Π_{33}^{SG} in both CTBLs are significant only very close to the surface where LES are known to have deficits. The contributions to Π_{22} behave similarly to the contributions to Π_{11} and are thus not shown separately.

Note that the turbulence-turbulence contribution exhibits the opposite sign compared to the total pressure-strain covariance and the other contributions in the upper part of the stratocumulus layer and near the surface (Figures 3b and 3d). This illustrates the different behavior of slow and fast pressure contributions. The slow terms Π_{33}^T and Π_{11}^T tend to return turbulence to isotropy "directly," by increasing (reducing) the vertical-velocity variance and reducing (increasing) the horizontal-velocity variance where the latter (former) variance dominates. The fast terms Π_{33}^B and Π_{11}^B lead to isotropization of the flow "indirectly." The term Π_{33}^B compensates part of the buoyancy production of the vertical-velocity variance and is in effect a sink term in the vertical-velocity variance budget. Therefore Π_{11}^B is in effect a source term in the horizontal-velocity variance budget (recall that $\Pi_{11}^B + \Pi_{22}^B + \Pi_{33}^B = 0$). The results shown in Figure 3 clearly demonstrate that modeling the total pressure-strain covariance Π_{ij} with the *Rotta* return-to-isotropy parameterization only (i.e., applying the return-to-isotropy parameterization to the entire pressure-scrambling term) may cause failure of a turbulence model since even the sign of Π_{ij} may not be obtained correctly.

Figure 4 shows Π_{13} and its components. Inside the subcloud layer of BOMEX, Π_{13}^T, Π_{13}^B and Π_{13}^S are of the same order of magnitude (Figure 4a). Inside the cumulus layer, the relative importance of the turbulence-turbulence contribution decreases, leaving the total pressure-strain covariance Π_{13} dominated by the mean shear and the buoyancy contributions. In DYCOMS (Figure 4b), the contributions Π_{13}^T, Π_{13}^B, and Π_{13}^S are roughly equally important throughout the boundary layer, including the cloud layer. Apart from the surface layer, the SGS contribution is negligibly small in both CTBLs. The vertical profiles of the contributions to Π_{23} are very similar to the vertical profiles of the contributions to Π_{13} and are thus not shown. The mean-shear, buoyancy, and turbulence-turbulence contributions to the Π_{12} component of the pressure-strain covariance are of similar importance in both BOMEX and DYCOMS (not shown).

3.3. Contributions to Pressure Gradient-Scalar Covariances

The pressure gradient-liquid water potential temperature covariance $\Pi_{\theta i}$ and the pressure gradient-total water specific humidity covariance Π_{qi} appear in the budget equations of the liquid water potential
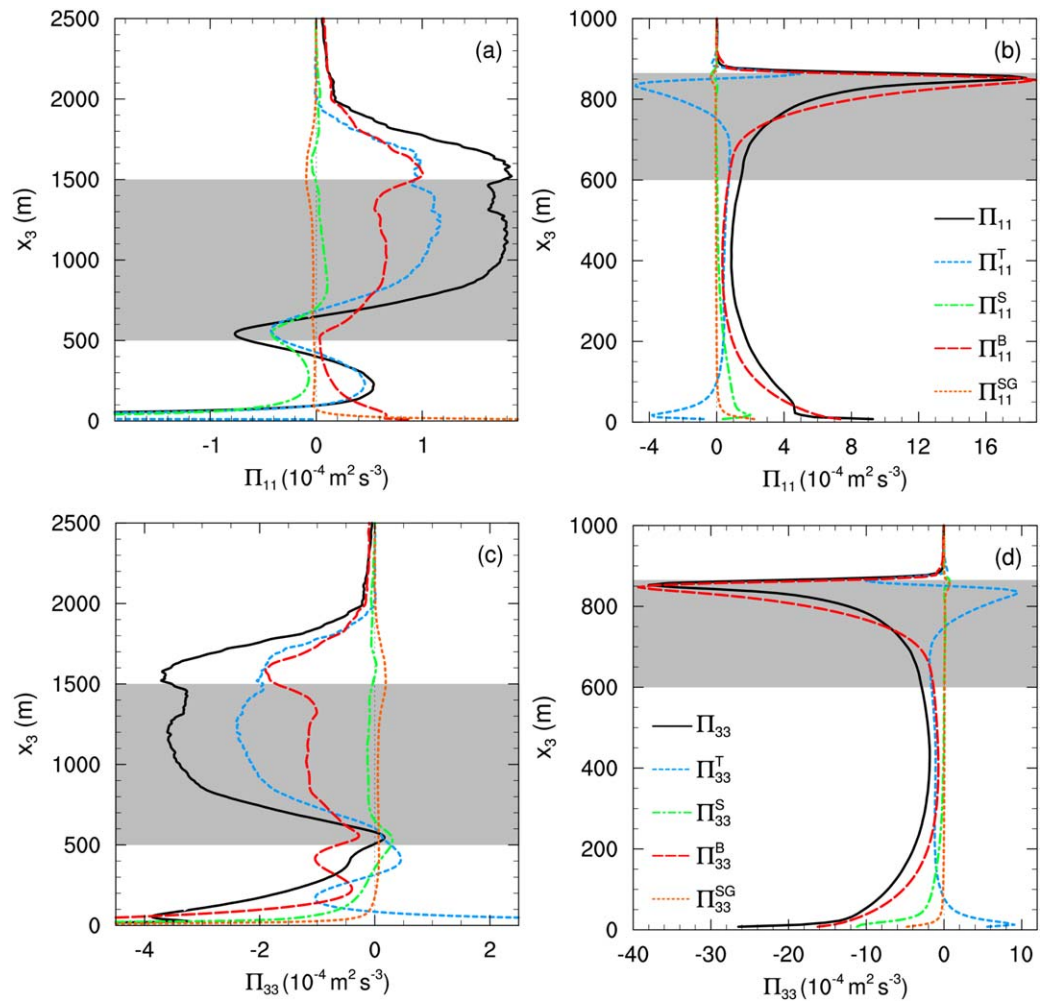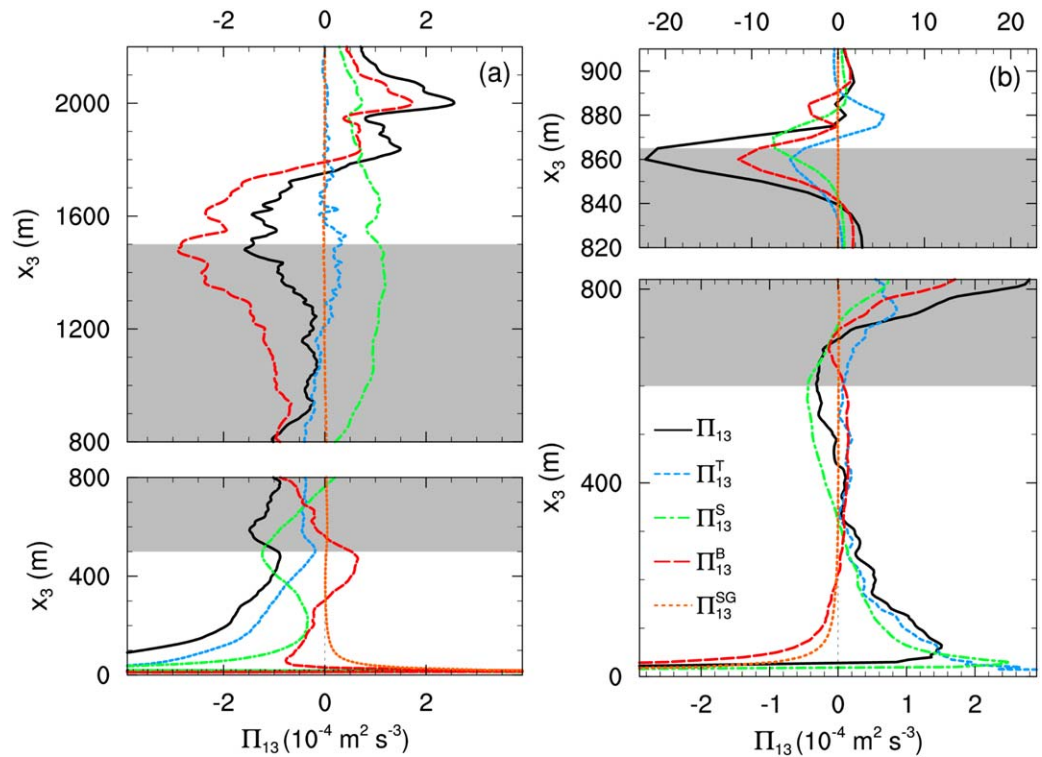
Figure 3. Vertical profiles of the pressure-strain covariance components Π_{11}, (a) and (b), and Π_{33}, (c) and (d), and of the contributions to Π_{11} and Π_{33} due to turbulence-turbulence interactions (T), mean shear (S), buoyancy (B), and subgrid model (SG). The BOMEX results are shown in Figures 3a and 3c, and the DYCOMS results are shown in Figures 3b and 3d. Legends refer to the plots in each row. Gray shading and time averaging as in Figure 1.

temperature flux and the total water-specific humidity flux, respectively. There is no strict analogy between the pressure-strain covariance Π_{ij} and the pressure gradient-scalar covariances $\Pi_{\theta i}$ and Π_{qi} in terms of redistribution since $\Pi_{\theta i}$ and Π_{qi} are vectors. The role of $\Pi_{\theta i}$ and Π_{qi} is in maintaining the second-moment budgets, however, it is similar to the role of Π_{ij}. In isotropic flows, the scalar fluxes vanish since a nonzero flux would imply a preferred direction and thus anisotropy. The pressure gradient-scalar covariances act to diminish both the magnitude of the scalar fluxes and the difference between the flux components by *scrambling* turbulent eddies [*Hanjalić and Launder*, 2011, p. 30].

The vertical components $\Pi_{\theta 3}$ and Π_{q3} of the pressure gradient-scalar covariances and the various contributions to $\Pi_{\theta 3}$ and Π_{q3} are shown in Figure 5. For both CTBLs, the total $\Pi_{\theta 3}$ is dominated by the buoyancy contribution $\Pi_{\theta 3}^{B}$ in the inversion layer (Figures 5a and 5b). By inversion layer, we refer to the interfacial layer located between the top of the cloud layer and the free troposphere, which is very thin (rather broad) in the DYCOMS (BOMEX) case where the temperature gradient at cloud top is strong (weak). Both the total covariance and the buoyancy contribution are up to two orders of magnitude higher than in the remainder of the boundary layer. The dominance of the buoyancy contribution is closely related to the vertical temperature-flux budget where buoyancy production in the inversion layer is the dominant production mechanism (cf. H15, Figures 9a and 9b). The buoyancy contribution to the pressure gradient–scalar covariance compensates a large part of the buoyancy production term and in effect acts to destroy the flux. In

Figure 4. Vertical profiles of the total pressure-strain covariance components Π_{13} for (a) BOMEX and (b) DYCOMS, and of the contributions to Π_{13} due to turbulence-turbulence interactions (T), mean shear (S), buoyancy (B), and subgrid model (SG). Ordinates are stretched near the cloud layer top. Different abscissa scales are used for the boundary layer in Figure 4b. Gray shading and time averaging as in Figure 1.

the lower part of both cloud layers and in the subcloud mixed layers, the turbulence-turbulence and the buoyancy contributions are of the same order of magnitude. The shear contribution $\Pi_{\theta 3}^{S}$ is much smaller than $\Pi_{\theta 3}^{T}$ and $\Pi_{\theta 3}^{B}$ even close to the surface. The contribution due to the SGS stress is small, confirming the fidelity of our LES results. The analysis of the vertical component of the pressure gradient-total water specific humidity covariance $\Pi_{q 3}$ yields similar results regarding the relative importance of the various contributions (Figures 5c and 5d). As in the BOMEX and DYCOMS cases, the predominance of the buoyancy contribution to the pressure gradient-scalar covariances in the inversion layer is also observed in dry convective boundary layers [*Moeng and Wyngaard*, 1986; *Mironov*, 2001].

The horizontal components of the pressure gradient-scalar covariances, $\Pi_{\theta 1}$, $\Pi_{q 1}$, $\Pi_{\theta 2}$, and $\Pi_{q 2}$ (not shown) are roughly equally composed of the turbulence-turbulence, shear, and buoyancy contributions in both CTBLs. Only very close to the surface the shear contribution becomes dominant.

The above analysis shows that $\Pi_{\theta i}$ and $\Pi_{q i}$ are analogous in terms of the relative importance of their various contributions. In the following sections, the LES results are presented for one scalar only (liquid water potential temperature). A discussion of models (parametrizations) of the pressure scrambling terms is given in terms of a "generic" pressure gradient-scalar covariance Π_{si}, where s stands for either θ_l or q_t.

3.4. Testing Models for Pressure Covariances

In the following, the pressure-scrambling terms estimated on the basis of LES data are used to test the applicability of some commonly used parameterizations to the boundary layers capped by shallow clouds. LES data are also used to estimate dimensionless constants in some closure relations.

Two models are tested in the present study. One is the basic model of *Rotta* [1951] and *Launder et al.* [1975] which is widely used in geophysical applications [e.g., *Zeman*, 1981; *Umlauf and Burchard*, 2005]. The parameterizations of the rapid pressure terms, i.e., the pressure terms due to buoyancy, mean shear, and Coriolis effects, are linear in the Reynolds stress and scalar flux. The parameterization of the turbulence-turbulence contribution (slow pressure term) is based on the *Rotta* return-to-isotropy model.
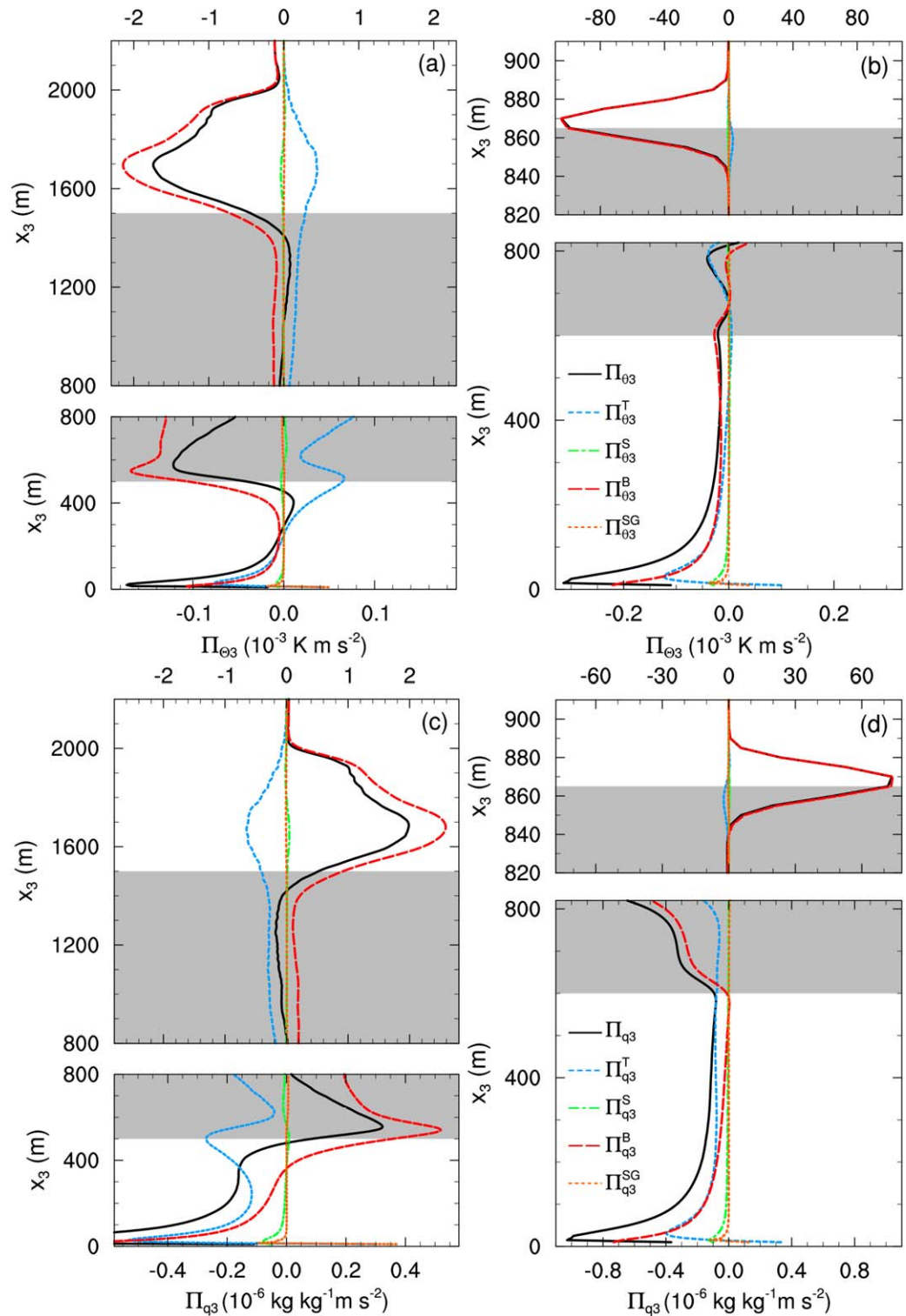
Figure 5. Vertical profiles of the total pressure gradient-scalar covariances $\Pi_{\theta 3}$, (a) and (b), and Π_{q3}, (c) and (d), and of the respective contributions due to turbulence-turbulence interactions (T), mean shear (S), buoyancy (B), and subgrid model (SG). The BOMEX results are shown in Figures 5a and 5c, and the DYCOMS results are shown in Figures 5b and 5d. Legends refer to the plots in each row. Ordinates are stretched near the cloud layer top. Different abscissa scales are used for the lower and upper part of the boundary layer. Gray shading and time averaging as in Figure 1.

Apart from simple linear models, various nonlinear models of the pressure-scrambling terms have been developed to date. A detailed overview is given, for example, by *Hanjalić and Launder* [2011]. In this study, the *Craft et al.* [1996] model of the buoyancy and turbulence-turbulence contributions is tested. The model is nonlinear in the Reynolds stress and scalar flux. It satisfies the so-called two-component limit (TCL). The TCL is the limit which turbulence approaches if the velocity component in one direction vanishes (and all turbulence moments including the velocity fluctuation in that direction vanish as well). Atmospheric turbulence approaches the TCL close to solid walls (e.g., the Earth's surface) and in strongly stable layers [e.g., *Zeman*, 1981], where vertical motions are strongly suppressed. By applying the TCL constraint, a realizable model can be constructed, which ensures, among other things, that velocity variances remain positive-definite or correlation coefficients cannot become larger than one [see *Craft et al.*, 1996, for details]. The *Craft et al.* [1996] model is referred to as the TCL model in what follows.

In both the basic model and the TCL model, the dimensionless departure-from-isotropy tensor is used. It is defined as

$$a_{ij} = \frac{\langle \bar{u}_i'' \bar{u}_j'' \rangle + \langle \tau_{ij} \rangle}{E} - \frac{2}{3} \delta_{ij}, \tag{17}$$

where $E = \frac{1}{2} \langle \bar{u}_i''^2 \rangle + \langle e \rangle$ is the total (resolved + subgrid) TKE. The departure-from-isotropy tensor is a measure of the flow anisotropy. In the isotropic limit, all components of a_{ij} are zero. Note that the parameterizations of the pressure-scrambling terms considered in the present study are cast in terms of quantities computed with the LES code. For example, the total TKE is a sum of the resolved TKE and the SGS TKE. It is the sum of these resolved and SGS parts that is treated as an LES-based approximation of the ensemble-mean TKE. The same holds for other turbulent quantities that enter the parameterizations considered here.

The basic model, which will be explained in detail in the following subsections, contains several dimensionless constants. The numerical values of most of these constants are fixed by mathematical constraints. In practice, however, those model constants are often treated as disposable parameters whose values are adjusted to improve the overall performance of a turbulence model in a particular flow regime. This route is also taken here and a least-square method is applied to determine best-fit values for the model constants. The method is explained in Appendix B.

As the contributions to the pressure-strain and pressure gradient-scalar covariances due to turbulence-turbulence interactions T, buoyancy B and mean shear S are the most important ones in our cloudy boundary-layer cases (Figures 3–5), tests of models of these contributions are presented. Recall that the results of the pressure gradient-scalar covariance tests are only shown exemplary for the pressure gradient-liquid water potential temperature covariance $\Pi_{\theta i}$.

3.4.1. Contributions Due to Turbulence-Turbulence Interactions

The *Rotta* relaxation parameterization is used in the basic model for the turbulence-turbulence contribution to the pressure-strain covariance. *Rotta* [1951] proposed that the return of turbulence to the isotropic state is proportional to the degree of anisotropy and it occurs on a certain time scale called the return-to-isotropy time scale. The return-to-isotropy parameterization used in the present study reads

$$\Pi_{ij}^{\mathrm{T}} = -\frac{C_{\mathrm{T}}^{\mathsf{u}}}{\tau_{\mathrm{E}}} a_{ij} E, \tag{18}$$

where $\tau_{\mathrm{E}} = E/\langle \epsilon \rangle$ is the TKE dissipation time scale, ϵ being the TKE dissipation rate, and $C_{\mathrm{T}}^{\mathsf{u}}$ being a dimensionless constant. Note that the return-to-isotropy time scale should enter equation (18), not the TKE dissipation time scale. However, it is commonly assumed in geophysical and engineering applications that the two time scales are proportional to each other. Values of $C_{\mathrm{T}}^{\mathsf{u}}$ are determined empirically and therefore depend on the situation studied. *Hanjalić and Launder* [2011, p. 67] provide a range of $1.5 < C_{\mathrm{T}}^{\mathsf{u}} < 1.8$. Based on atmospheric boundary layer simulations, *Zeman* [1981] determined a range of $1 \leq C_{\mathrm{T}}^{\mathsf{u}} \leq 3$.

The *Rotta* approach was extended to the pressure gradient–scalar covariance by *Monin* [1965]. The relaxation (return-to-isotropy) approximation for the turbulence-turbulence contribution reads

$$\Pi_{si}^{\mathsf{T}} = -\frac{C_{\mathsf{T}}^{\mathsf{s}}}{\tau_{\mathsf{E}}}\left(\langle\bar{u}_i''\bar{s}''\rangle + \langle\tau_{si}\rangle\right),\tag{19}$$

where τ_{si} denotes the SGS scalar flux computed by the LES model. Equation (19) suggests that the fluctuating pressure acts to destroy the scalar flux on a certain relaxation (return-to-isotropy) time scale. As with equation (18), the scalar-flux return-to-isotropy time scale is assumed to be proportional to the TKE dissipation time scale. According to *Zeman* [1981], the values of $C_{\mathsf{T}}^{\mathsf{s}}$ lie between 3 and 5. For dry convective boundary layers, an estimate of $C_{\mathsf{T}}^{\mathsf{s}}=3.0$ was obtained on the basis of LES data [e.g., *Mironov*, 2001].

There are numerous more complex models of Π_{ij}^{T} that are nonlinear in a_{ij} and $\langle\bar{u}_i''\bar{s}''\rangle$. Dimensionless coefficients appearing in those models are either constants or functions of scalar invariants of tensors characterizing the problem in question, e.g., the departure-from-isotropy tensor a_{ij} [*Lumley*, 1978]. The TCL model of *Craft et al.* [1996] uses the following expression for the turbulence-turbulence contribution to the pressure–strain covariance:

$$\Pi_{ij}^{\mathsf{T}} = -\frac{C_{\mathsf{T}1}^{\mathsf{u}}}{\tau_{\mathsf{E}}}\left[a_{ij} + C_{\mathsf{T}2}^{\mathsf{u}}\left(a_{ik}a_{jk} - \frac{1}{3}A_2\delta_{ij}\right)\right]E,\tag{20}$$

where $C_{\mathsf{T}1}^{\mathsf{u}} = \left(3.75A_2^{1/2}+1\right)A$, $C_{\mathsf{T}2}^{\mathsf{u}}=0.7$, $A_2=a_{ij}a_{ji}$, and $A_3=a_{ij}a_{jk}a_{ki}$ are the invariants of a_{ij}, and A is the so-called flatness parameter defined as $A=1-\frac{9}{8}(A_2-A_3)$.

The TCL parameterization for the turbulence-turbulence contribution to the pressure gradient-scalar covariance reads [*Craft et al.*, 1996]

$$\Pi_{si}^{\mathsf{T}} = -C_{\mathsf{T}1}^{\mathsf{s}}\,\frac{R^{1/2}}{\tau_{\mathsf{E}}}\left[\left(\langle\bar{u}_i''\bar{s}''\rangle + \langle\tau_{si}\rangle\right)\left(1+C_{\mathsf{T}2}^{\mathsf{s}}A_2\right)+C_{\mathsf{T}3}^{\mathsf{s}}\,a_{ij}\left(\langle\bar{u}_j''\bar{s}''\rangle + \langle\tau_{sj}\rangle\right)\right.$$
$$\left.+C_{\mathsf{T}4}^{\mathsf{s}}\,a_{ij}a_{jk}\left(\langle\bar{u}_k''\bar{s}''\rangle + \langle\tau_{sk}\rangle\right)\right]+C_{\mathsf{T}5}^{\mathsf{s}}\,R\,E\,a_{ij}\,\frac{\partial\langle\bar{s}\rangle}{\partial x_j}.\tag{21}$$

The dimensionless parameters in (21) are $C_{\mathsf{T}1}^{\mathsf{s}}=1.7\left[1+1.2(A_2A)^{1/2}\right]$, $C_{\mathsf{T}2}^{\mathsf{s}}=0.6$, $C_{\mathsf{T}3}^{\mathsf{s}}=-0.8$, $C_{\mathsf{T}4}^{\mathsf{s}}=1.1$, and $C_{\mathsf{T}5}^{\mathsf{s}}=0.2A^{1/2}$. $R=\tau_{\mathsf{E}}/\tau_{\mathsf{s}}$ is the ratio of the dissipation time-scales for the TKE and for the scalar variance. The scalar variance dissipation time-scale is defined as $\tau_{\mathsf{s}}=\frac{1}{2}(\langle\bar{s}''^2\rangle + \langle\varsigma\rangle)/\langle\epsilon_{\mathsf{s}}\rangle$, where ς is the SGS scalar variance, and ϵ_{s} is the scalar-variance dissipation rate. The latter quantities are estimated as $\varsigma=5\tau_{si}^2/e$ and $\epsilon_{\mathsf{s}}=K_{\mathsf{h}}(\partial\bar{s}/\partial x_i)^2$, where K_{h} is the SGS eddy diffusivity (see H15 for details).

In Figure 6, the turbulence-turbulence contributions Π_{11}^{T}, Π_{33}^{T}, and Π_{13}^{T} from LES are compared with their parameterizations through equations (18) and (20). The TKE dissipation rate $\langle\epsilon\rangle$ is estimated as a residual of the total (resolved + subgrid) TKE budget as described in H15. Apart from the estimate of $C_{\mathsf{T}}^{\mathsf{u}}=2.0$ which is in the typical range given by *Zeman* [1981], we use the best-fit values of $C_{\mathsf{T}}^{\mathsf{u}}$ obtained by the least-square method described in the Appendix B. Following *Mironov* [2001], the SGS contribution to the pressure-strain covariance, $\mathcal{P}_{ij}$ (see section 2.2 and Appendix B in H15), is added to the turbulence-turbulence part of the resolved pressure-strain covariance. In the remainder of this paper, Π_{ij}^{T} denotes the sum of the resolved and SGS contributions.

Figure 6 shows that the results obtained with the *Rotta* model and with the TCL model hardly differ. Over most of the boundary layer, both parameterizations are able to reproduce the shape of the LES-based profiles quite accurately. However, both models underestimate the diagonal components Π_{11}^{T} and Π_{33}^{T} in the cumulus layer (Figures 6a and 6c). At the top of the stratocumulus layer, both models have problems in reproducing some maxima and minima (Figures 6b, 6d, and 6f). The best-fit values of $C_{\mathsf{T}}^{\mathsf{u}}$ and their root-mean-square error (RMSE) are provided for all components of the pressure-strain tensor in Table 1. Considering the RMSE, almost all values of $C_{\mathsf{T}}^{\mathsf{u}}$ are within the range $1 \leq C_{\mathsf{T}}^{\mathsf{u}} \leq 3$ known from literature. The estimates in Table 1 differ among the six components of the pressure-strain tensor and among the two CTBLs. There is no universal best-fit estimate for $C_{\mathsf{T}}^{\mathsf{u}}$ that is valid for both cloudy boundary layers and for all spatial directions. However, since the spread of $C_{\mathsf{T}}^{\mathsf{u}}$ values is rather small, using the value of $C_{\mathsf{T}}^{\mathsf{u}}=1.7$ would provide a reasonable fit for most components.

Figure 7 compares $\Pi_{\theta3}^{\mathsf{T}}$ and $\Pi_{\theta1}^{\mathsf{T}}$ from the LES data with their parameterizations through equations (19) and (21). Similarly to the turbulence-turbulence contribution to the pressure-strain covariance, the SGS pressure-term $\mathcal{P}_{si}$ is added to Π_{si}^{T} (see H15 for details). The sum is denoted as Π_{si}^{T} in the following.
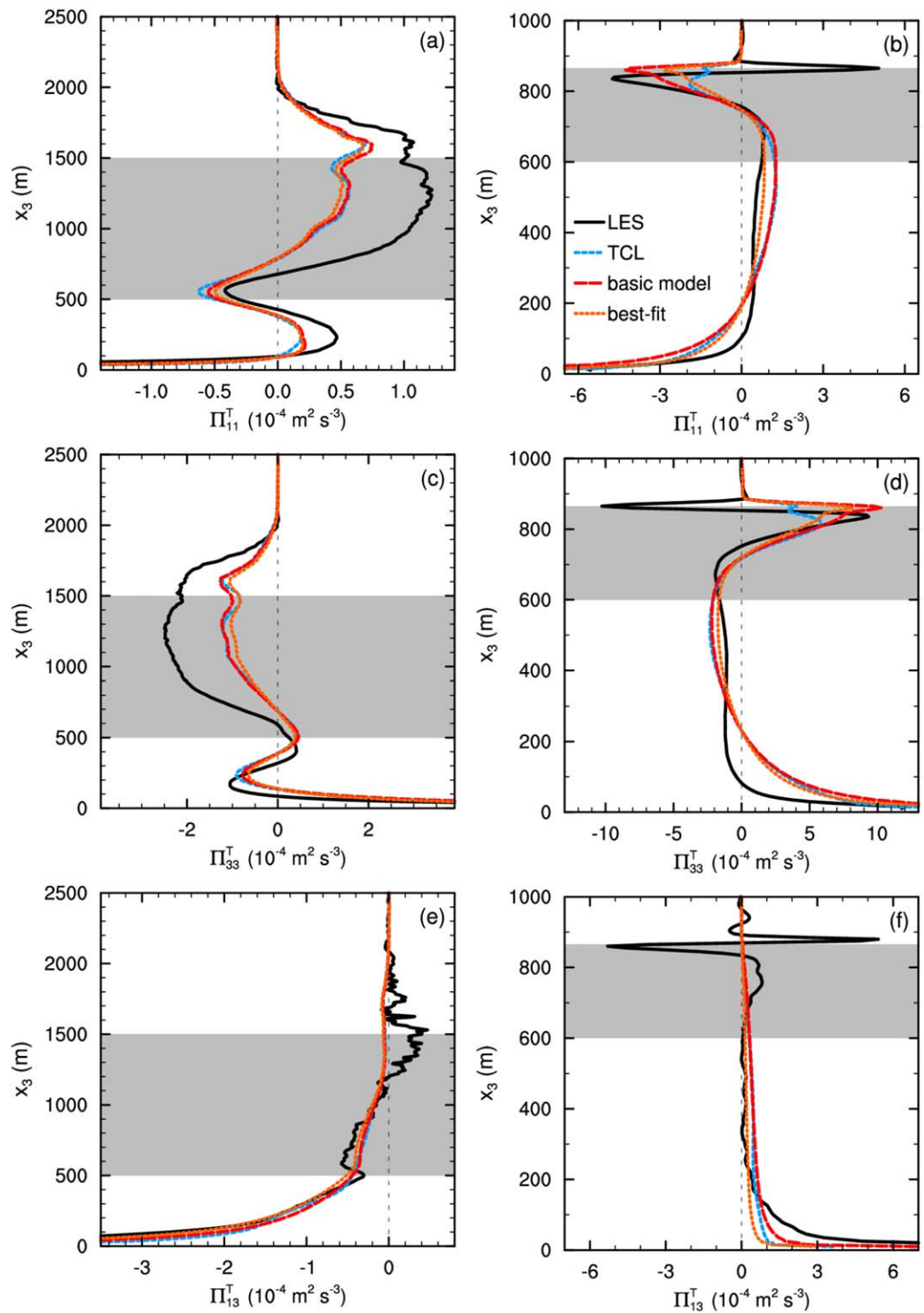
Figure 6. Vertical profiles of the turbulence-turbulence contribution to the pressure-strain covariance components Π_{11}^T, (a) and (b), Π_{33}^T, (c) and (d), and Π_{13}^T, (e) and (f). Solid black lines show Π_{11}^T, Π_{33}^T, and Π_{13}^T from LES data, short-dashed blue lines are based on the TCL model (20), and long-dashed red as well as dotted orange lines are based on the Rotta-type parameterization (18) of the basic model. The long-dashed red line is determined with $C_T^u = 2.0$, and the dotted orange line, by means of the best-fit value of C_T^u which is 1.81 in Figure 6a, 1.33 in Figure 6b, 1.67 in Figure 6c, 1.59 in Figure 6d, 2.32 in Figure 6e, and 0.87 in Figure 6f (Table 1). The BOMEX results are shown in Figures 6a, 6c, and 6e, and the DYCOMS results are shown in Figures 6b, 6d, and 6f. Gray shading and time averaging as in Figure 1.

Table 1. Best-Fit Estimates of C_T^u [a]

	Π_{11}^T	Π_{22}^T	Π_{33}^T	Π_{12}^T	Π_{13}^T	Π_{23}^T	Lit.
C_T^u (B)	1.81 ± 1.08	1.99 ± 1.55	1.67 ± 1.30	1.29 ± 1.37	2.32 ± 1.23	2.38 ± 1.47	1–3
C_T^u (D)	1.33 ± 0.78	1.72 ± 1.08	1.59 ± 0.94	1.13 ± 0.66	0.87 ± 0.70	2.57 ± 0.28	1–3

[a] Best-fit estimates of the model constant C_T^u of the Rotta-type parameterization (18) including root-mean-square error (RMSE) for BOMEX (B) and DYCOMS (D). Linear regression is used for fitting. Literature values (Lit.) stem from *Zeman* [1981].

In Figure 7, $C_T^s = 3.0$ is used. The *Rotta*-type and the TCL parameterizations of $\Pi_{\theta 3}^T$ agree satisfactorily with the LES data over most of the two boundary layers except near the cloud top, where (19) underestimates the LES data in both cases and (21) overestimates (underestimates) the LES data near the stratocumulus (cumulus) top (Figures 7a and 7b). The local maximum at cumulus cloud base is completely missed by the *Rotta*-type model; the TCL model performs slightly better. Both the Rotta-type model and the TCL model reproduce the principal shape of the horizontal component $\Pi_{\theta 1}^T$ of the pressure gradient-liquid water potential temperature covariance (Figures 7c and 7d). Both models overestimate the LES data in the inversion layer, although the TCL model performs better in the stratocumulus case (Figure 7d). The best-fit estimates for C_T^s are given in Table 2. The best-fit values of C_T^s for the vertical components of the pressure gradient-scalar covariances do not differ strongly between the two scalars and between the two CTBLs. The values are roughly between 3 and 5 which is the range given by *Zeman* [1981]. Thus, one value for C_T^s can be used to model both $\Pi_{\theta 3}^T$ and Π_{q3}^T. The estimates of C_T^s for the horizontal components of the pressure gradient-scalar covariances show a larger spread and larger RMSE. Overall, this shows the restrictive character of the Rotta-type model.

3.4.2. Contributions Due to Buoyancy

In order to account for the buoyancy contribution to the pressure-strain covariance in the basic model, the so-called *isotropization of production* (IP) parameterization [*Naot et al.*, 1970] is used. The IP parameterization is linear in the second moments. It reads [e.g., *Hanjalić and Launder*, 2011, p. 119]

$$\Pi_{ij}^B = -C_B^u \left(\mathcal{B}_{ij} - \frac{1}{3}\delta_{ij}\mathcal{B}_{kk} \right)$$

$$= -C_B^u \left[\frac{g}{\theta_0}\delta_{i3}\left(\left\langle \bar{u}_j''\bar{\theta}_v'' \right\rangle + \left\langle \tau_{vj} \right\rangle \right) + \frac{g}{\theta_0}\delta_{j3}\left(\left\langle \bar{u}_i''\bar{\theta}_v'' \right\rangle + \left\langle \tau_{vi} \right\rangle \right) - \frac{2}{3}\delta_{ij}\frac{g}{\theta_0}\delta_{k3}\left(\left\langle \bar{u}_k''\bar{\theta}_v'' \right\rangle + \left\langle \tau_{vk} \right\rangle \right) \right],$$

(22)

where $\mathcal{B}_{ij} = \frac{g}{\theta_0}\delta_{i3}\left(\left\langle \bar{u}_j''\bar{\theta}_v'' \right\rangle + \left\langle \tau_{vj} \right\rangle \right) + \frac{g}{\theta_0}\delta_{j3}\left(\left\langle \bar{u}_i''\bar{\theta}_v'' \right\rangle + \left\langle \tau_{vi} \right\rangle \right)$ denotes the buoyancy production/destruction term in the Reynolds-stress budget equation [H15, equation (1)]. Estimates of C_B^u reported in the literature are in the range $0.3 \leq C_B^u \leq 0.6$, where $C_B^u = \frac{3}{10}$ can be derived analytically in the case of isotropic turbulence [e.g., *Hanjalić and Launder*, 2011, p. 120].

Analogously to equation (22), the IP parameterization for the buoyancy contribution to the pressure gradient-scalar covariance is

$$\Pi_{si}^B = -C_B^s \mathcal{B}_{si} = -C_B^s \frac{g}{\theta_0}\delta_{i3}\left(\left\langle \bar{s}''\bar{\theta}_v'' \right\rangle + \left\langle \tau_{vs} \right\rangle \right),$$

(23)

where $\mathcal{B}_{si} = \frac{g}{\theta_0}\delta_{i3}\left(\left\langle \bar{s}''\bar{\theta}_v'' \right\rangle + \left\langle \tau_{vs} \right\rangle \right)$ is the buoyancy production/destruction term in the scalar-flux budget (H15, equation (3)). The way of estimating the SGS scalar-virtual potential temperature covariance $\tau_{vs} = \overline{s'\theta_v'}$ is explained in detail in H15. In the IP parameterizations (22) and (23), the pressure-scrambling terms due to buoyancy are set proportional to the buoyancy terms in the Reynolds-stress and scalar-flux budgets, respectively. Therefore, the buoyancy contributions to the pressure-scrambling terms simply compensate a part of the buoyancy production/destruction of the Reynolds stress and scalar fluxes. A theoretical value of the dimensionless constant C_B^s that stems from isotropic tensor modeling is 1/3 [see e.g., *Lumley*, 1978; *Zeman*, 1981; *Hanjalić and Launder*, 2011]. *Moeng and Wyngaard* [1986] found, however, that the value of $C_B^s = 0.5$ is more consistent with data from LES of a slightly sheared, dry convective boundary layer.
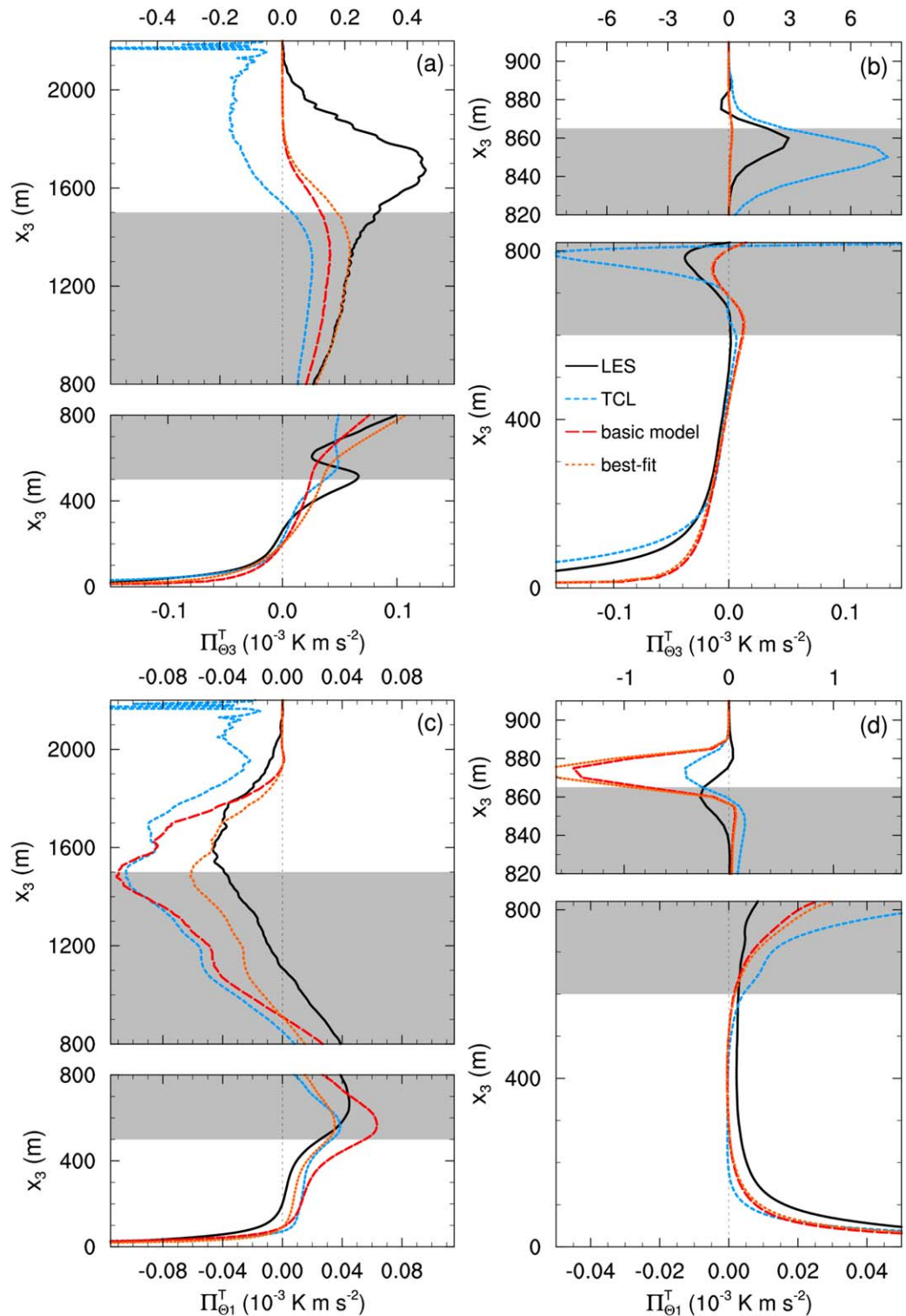
Figure 7. Vertical profiles of the turbulence-turbulence contribution to the vertical $\Pi^T_{\theta 3}$, (a) and (b), and horizontal $\Pi^T_{\theta 1}$, (c) and (d), components of the pressure gradient-liquid water potential temperature covariance. Solid black lines show $\Pi^T_{\theta 3}$ and $\Pi^T_{\theta 1}$ from LES data, short-dashed blue lines are based on the TCL model (21), and long-dashed red and dotted orange lines are based on the Rotta-type parameterization (19) of the basic model. The long-dashed red line is determined with $C^s_1 = 3.0$, and the dotted orange line, by means of the best-fit value of C^s_1 which is 4.26 in Figure 7a, 3.25 in Figure 7b, 1.66 in Figure 7c, and 3.50 in Figure 7d (Table 2). The BOMEX results are shown in Figure 7a and 7c, and the DYCOMS results are shown in Figures 7b and 7d. Ordinates are stretched near the cloud layer top. Different abscissa scales are used for the lower and upper part of the boundary layers in Figures 7a, 7b, and 7d. Gray shading and time averaging as in Figure 1.

Table 2. Best-Fit Estimates of C_T^s [a]

	$\Pi_{\theta 1}^T$	$\Pi_{\theta 2}^T$	$\Pi_{\theta 3}^T$	Π_{q1}^T	Π_{q2}^T	Π_{q3}^T	Lit.
C_T^s (B)	1.66 ± 1.45	1.44 ± 1.23	4.26 ± 1.54	1.75 ± 1.31	1.31 ± 1.08	4.13 ± 1.30	3–5
C_T^s (D)	3.50 ± 2.38	3.89 ± 1.42	3.25 ± 2.29	1.45 ± 0.86	1.11 ± 0.62	2.86 ± 0.64	3–5

[a]As in Table 1 but for the model constant C_T^s used in (19).

The TCL parameterization of the buoyancy contribution to Π_{ij} is

$$
\begin{aligned}
\Pi_{ij}^B = & -\left(\frac{3}{10}+\frac{3A_2}{80}\right)\left(\mathcal{B}_{ij}-\frac{1}{3}\delta_{ij}\mathcal{B}_{kk}\right)+\frac{1}{6}\,a_{ij}\,\mathcal{B}_{kk} \\
& +\frac{2}{15}\frac{g}{\theta_0}\left(\left\langle\bar{u}_m''\bar{\theta}_v''\right\rangle+\left\langle\tau_{vm}\right\rangle\right)(\delta_{i3}\,a_{mj}+\delta_{j3}\,a_{mi}) \\
& -\frac{1}{3}\frac{g}{\theta_0}\delta_{k3}\left[a_{ik}\left(\left\langle\bar{u}_j''\bar{\theta}_v''\right\rangle+\left\langle\tau_{vj}\right\rangle\right)+a_{jk}\left(\left\langle\bar{u}_i''\bar{\theta}_v''\right\rangle+\left\langle\tau_{vi}\right\rangle\right)\right] \\
& +\frac{1}{10}\frac{g}{\theta_0}\delta_{ij}\,\delta_{k3}\,a_{mk}\left(\left\langle\bar{u}_m''\bar{\theta}_v''\right\rangle+\left\langle\tau_{vm}\right\rangle\right) \\
& +\frac{1}{4}\frac{g}{\theta_0}\delta_{k3}\,a_{ij}\,a_{mk}(\left\langle\bar{u}_m''\bar{\theta}_v''\right\rangle+\left\langle\tau_{vm}\right\rangle) \\
& +\frac{1}{8}\frac{g}{\theta_0}\left(\delta_{k3}[a_{ki}\,a_{mj}+a_{kj}\,a_{mi}]\left(\left\langle\bar{u}_m''\bar{\theta}_v''\right\rangle+\left\langle\tau_{vm}\right\rangle\right)\right. \\
& \left.-\delta_{k3}\,a_{mk}\left[a_{mj}\left(\left\langle\bar{u}_i''\bar{\theta}_v''\right\rangle+\left\langle\tau_{vi}\right\rangle\right)+a_{mi}\left(\left\langle\bar{u}_j''\bar{\theta}_v''\right\rangle+\left\langle\tau_{vj}\right\rangle\right)\right]\right) \\
& -\frac{3}{40}\frac{g}{\theta_0}\left(\left[a_{mk}\left(\left\langle\bar{u}_k''\bar{\theta}_v''\right\rangle+\left\langle\tau_{vk}\right\rangle\right)(\delta_{i3}\,a_{mj}+\delta_{j3}\,a_{mi})\right]\right. \\
& \left.-\frac{2}{3}\delta_{ij}\,\delta_{k3}\,a_{mk}\,a_{mn}\left(\left\langle\bar{u}_n''\bar{\theta}_v''\right\rangle+\left\langle\tau_{vn}\right\rangle\right)\right).
\end{aligned}
\tag{24}
$$

This parameterization is taken from *Hanjalić and Launder* [2011, p. 123] and is based on *Craft et al.* [1996]. In the isotropic limit where $a_{ij}=0$, equation (24) reduces to the IP parameterization (22) with $C_B^u=\frac{3}{10}$.

The TCL parameterization [*Craft et al.*, 1996] of the buoyancy contribution to Π_{si} reads

$$
\Pi_{si}^B=-\left(\frac{1}{3}\delta_{ik}-a_{ik}\right)\mathcal{B}_{sk}=-\left(\frac{1}{3}\delta_{ik}-a_{ik}\right)\frac{g}{\theta_0}\delta_{k3}\left(\left\langle\bar{s}''\bar{\theta}_v''\right\rangle+\left\langle\tau_{vs}\right\rangle\right).
\tag{25}
$$

It differs to the IP parameterization (23) by the nonconstant factor $\left(\frac{1}{3}\delta_{ik}-a_{ik}\right)$. Note that (25) gives nonzero contributions to the horizontal components ($i\neq 3$) of Π_{si}^B, which the IP model (23) does not.

Three components of the buoyancy contribution Π_{ij}^B to the pressure-strain tensor computed from (22) and (24) are compared with the LES data in Figure 8. A value of $C_B^u=\frac{3}{10}$ and the best-fit estimates of C_B^u are used. For the diagonal components Π_{11}^B and Π_{33}^B (Figures 8a–8d), the linear IP model with $C_B^u=3/10$ and the nonlinear TCL model give similar results over most of both CTBLs. Both models do a reasonable job but leave room for improvement in agreeing with LES data. Both the IP and the TCL model strongly underestimate the peaks of Π_{11}^B and Π_{33}^B at the top of the stratocumulus layer (Figures 8b and 8d). The linear profiles of Π_{11}^B and Π_{33}^B computed from (22) and (24) in the subcloud layers of BOMEX and DYCOMS are eye-catching. This can be attributed to the proportionality of (22) to the buoyancy production/destruction term $\mathcal{B}_{ij}$. The diagonal components $\mathcal{B}_{11}$ and $\mathcal{B}_{22}$ are both zero, leaving $\mathcal{B}_{33}$ to be the only nonzero diagonal contribution in (22). $\mathcal{B}_{33}$ is proportional to the vertical buoyancy flux which shows a linear decrease with height in the subcloud layer of both CTBLs (cf. H15). However, Π_{11}^B (Π_{33}^B) computed by the LES model do not decrease (increase) linearly with height in the subcloud layer. Compared to the diagonal components, the models of the off-diagonal component Π_{13}^B show closer agreement with LES data (Figures 8e and 8f). Except for the surface layer, both models are able to reproduce the shape of the LES-based profiles quite well.

Table 3 presents the best-fit estimates of C_B^u. They are all smaller than one as the IP parameterization requires. The range of best-fit values is larger than the range of $0.3\leq C_B^u\leq 0.6$ given in literature. High RMSEs are also present. The best-fit estimates of C_B^u are lower for DYCOMS than for BOMEX.
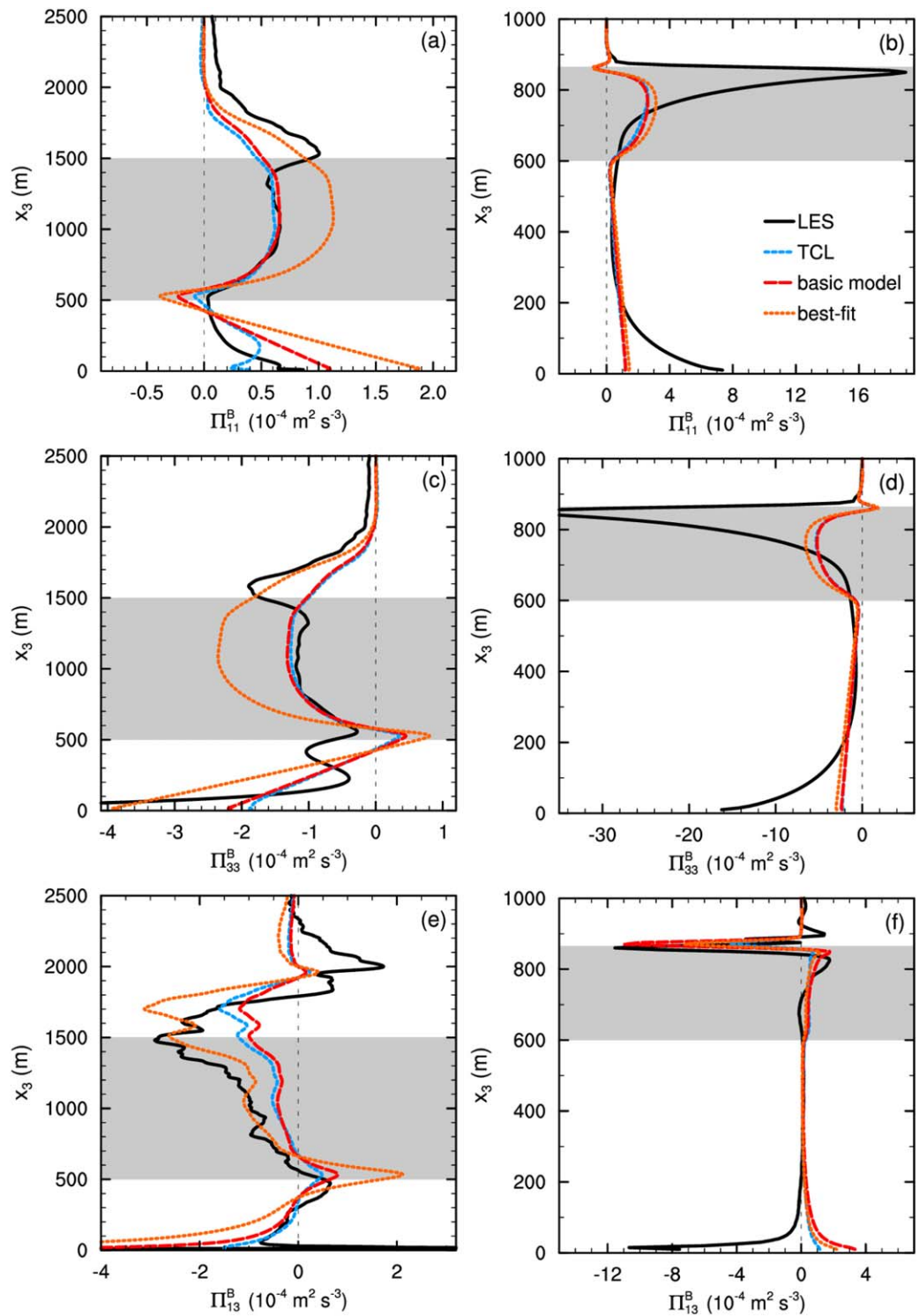
Figure 8. Vertical profiles of the buoyancy contribution to the pressure-strain covariance components Π_{11}^B, (a) and (b), Π_{33}^B, (c) and (d), and Π_{13}^B, (e) and (f). Solid black lines show Π_{11}^B, Π_{33}^B, and Π_{13}^B from LES data, short-dashed blue lines are based on the TCL model (24), and long-dashed red and dotted orange lines are based on the IP parameterization (22) of the basic model. The long-dashed red line is determined with $C_B^u = \frac{3}{10}$, and the dotted orange line, by means of the best-fit value of C_B^u which is 0.52 in Figure 8a, 0.36 in Figure 8b, 0.54 in Figure 8c, 0.38 in Figure 8d, 0.79 in Figure 8e, and 0.20 in Figure 8f (Table 3). The BOMEX results are shown in Figures 8a, 8c, and 8e, and the DYCOMS results are shown in Figures 8b, 8d, and 8f. Grey shading and time averaging as in Figure 1.

Table 3. Best-Fit Estimates of C_B^u [a]

	Π_{11}^B	Π_{22}^B	Π_{33}^B	Π_{12}^B	Π_{13}^B	Π_{23}^B	Lit.
C_B^u (B)	0.52 ± 0.57	0.49 ± 0.59	0.54 ± 0.53	–	0.79 ± 0.60	0.77 ± 0.83	0.3–0.6
C_B^u (D)	0.36 ± 0.20	0.39 ± 0.20	0.38 ± 0.20	–	0.20 ± 0.15	0.38 ± 0.30	0.3–0.6

[a]As in Table 1 but for the model constant C_B^u used in the IP parameterization (22). Literature values (Lit.) are taken from *Hanjalić and Launder* [2011, S. 120]. Note that a fitting for the Π_{12}^B is not possible since (22) gives zero for this component.

Figure 9 compares the buoyancy components $\Pi_{\theta 3}^B$ and $\Pi_{\theta 1}^B$ computed from the parameterizations (23) and (25) with the LES data. The TCL model strongly underestimates $\Pi_{\theta 3}^B$ at the top of and above the cumulus layer (Figure 9a). It overestimates $\Pi_{\theta 3}^B$ near the stratocumulus top and underestimates it in the upper part of the subcloud layer (Figure 9b). The IP model is able to reproduce the LES-based profile quite accurately in the BOMEX case. In the DYCOMS case, the IP model noticeably underestimates the LES data near the top of the stratocumulus layer (Figure 9b). As regards the vertical pressure gradient-scalar covariance, a simple IP model (with the best-fit value of a dimensionless model constant) proves to perform better than a more sophisticated TCL model. This is in line with *Mironov* [2001] who observed a similar behavior in a dry convective boundary layer. The best-fit estimates of the model constant C_B^s are very close to 0.5 for both CTBLs and for both scalars (see Table 4). This corroborates the findings of *Moeng and Wyngaard* [1986] and *Mironov* [2001] who found 0.5 to be an optimal value of C_B^s for the dry convective boundary layer. If the IP parameterization (23) with $C_B^s = 0.5$ is used, the buoyancy contribution Π_{s3}^B offsets one half of the buoyancy production in the scalar-flux budget.

The horizontal buoyancy component $\Pi_{\theta 1}^B$ computed from (23) and (25) and from LES are shown in Figures 9c and 9d for both CTBLs. Note that (23) yields a nonzero value for the vertical component Π_{s3}^B of Π_{si}^B (aligned with the vector of gravity) only. The linear parameterization (23) is unable to account for the horizontal components ($i = 1$ and $i = 2$) of Π_{si}^B. This is obviously at variance with our LES data showing that the horizontal buoyancy contributions to Π_{si} are of the same order of magnitude as the shear and as the turbulence-turbulence contributions. Thus, the IP model should not be used to model the buoyancy contribution to the horizontal pressure gradient-scalar covariance. As seen from Figures 9c and 9d, the TCL model is able to give an order-of-magnitude estimate of $\Pi_{\theta 1}^B$ but it fails in reproducing the shape of the LES-based profiles.

3.4.3. Contributions Due to Mean Velocity Shear

Within the framework of the basic model, the contribution due to mean velocity shear is accounted for by means of the IP parameterization. The IP parameterization for the pressure-strain covariance reads

$$
\begin{aligned}
\Pi_{ij}^S &= -C_S^u \left(\mathcal{G}_{ij} - \frac{1}{3} \delta_{ij} \mathcal{G}_{kk} \right) \\
&= C_S^u \left[\left(\langle \bar{u}_j'' \bar{u}_k'' \rangle + \langle \tau_{jk} \rangle \right) \frac{\partial \langle \bar{u}_i \rangle}{\partial x_k} + \left(\langle \bar{u}_i'' \bar{u}_k'' \rangle + \langle \tau_{ik} \rangle \right) \frac{\partial \langle \bar{u}_j \rangle}{\partial x_k} - \frac{2}{3} \delta_{ij} \left(\langle \bar{u}_k'' \bar{u}_l'' \rangle + \langle \tau_{kl} \rangle \right) \frac{\partial \langle \bar{u}_k \rangle}{\partial x_l} \right],
\end{aligned}
\tag{26}
$$

where $\mathcal{G}_{ij} = -\left[\left(\langle \bar{u}_j'' \bar{u}_k'' \rangle + \langle \tau_{jk} \rangle \right) \frac{\partial \langle \bar{u}_i \rangle}{\partial x_k} + \left(\langle \bar{u}_i'' \bar{u}_k'' \rangle + \langle \tau_{ik} \rangle \right) \frac{\partial \langle \bar{u}_j \rangle}{\partial x_k} \right]$ is the mean shear production/destruction term in the Reynolds-stress budget equation. The model constant C_S^u is usually taken to be equal to $\frac{3}{5}$ [*Hanjalić and Launder*, 2011, p. 68].

The IP parameterization for the shear contribution to the pressure gradient-scalar covariance reads

$$
\Pi_{si}^S = -C_S^s \, \mathcal{G}_{si}^u = C_S^s \left(\langle \bar{u}_k'' \bar{s}'' \rangle + \langle \tau_{sk} \rangle \right) \frac{\partial \langle \bar{u}_i \rangle}{\partial x_k},
\tag{27}
$$

where $\mathcal{G}_{si}^u = -\left(\langle \bar{u}_k'' \bar{s}'' \rangle + \langle \tau_{sk} \rangle \right) \partial \langle \bar{u}_i \rangle / \partial x_k$ is the production/destruction of scalar flux due to mean shear appearing in the scalar-flux budget (H15, equation (3)). The estimates of the model constant C_S^s lie in the range $0.4 \leq C_S^s \leq 0.55$ [*Hanjalić and Launder*, 2011, p. 68].

Equations (26) and (27) show that Π_{ij}^S and Π_{si}^S given by the IP parameterizations are proportional to the shear production/destruction terms in the Reynolds-stress and scalar-flux budgets, respectively. As C_S^u and C_S^s are positive and smaller than one, a part of the shear production is offset by the pressure-scrambling terms.
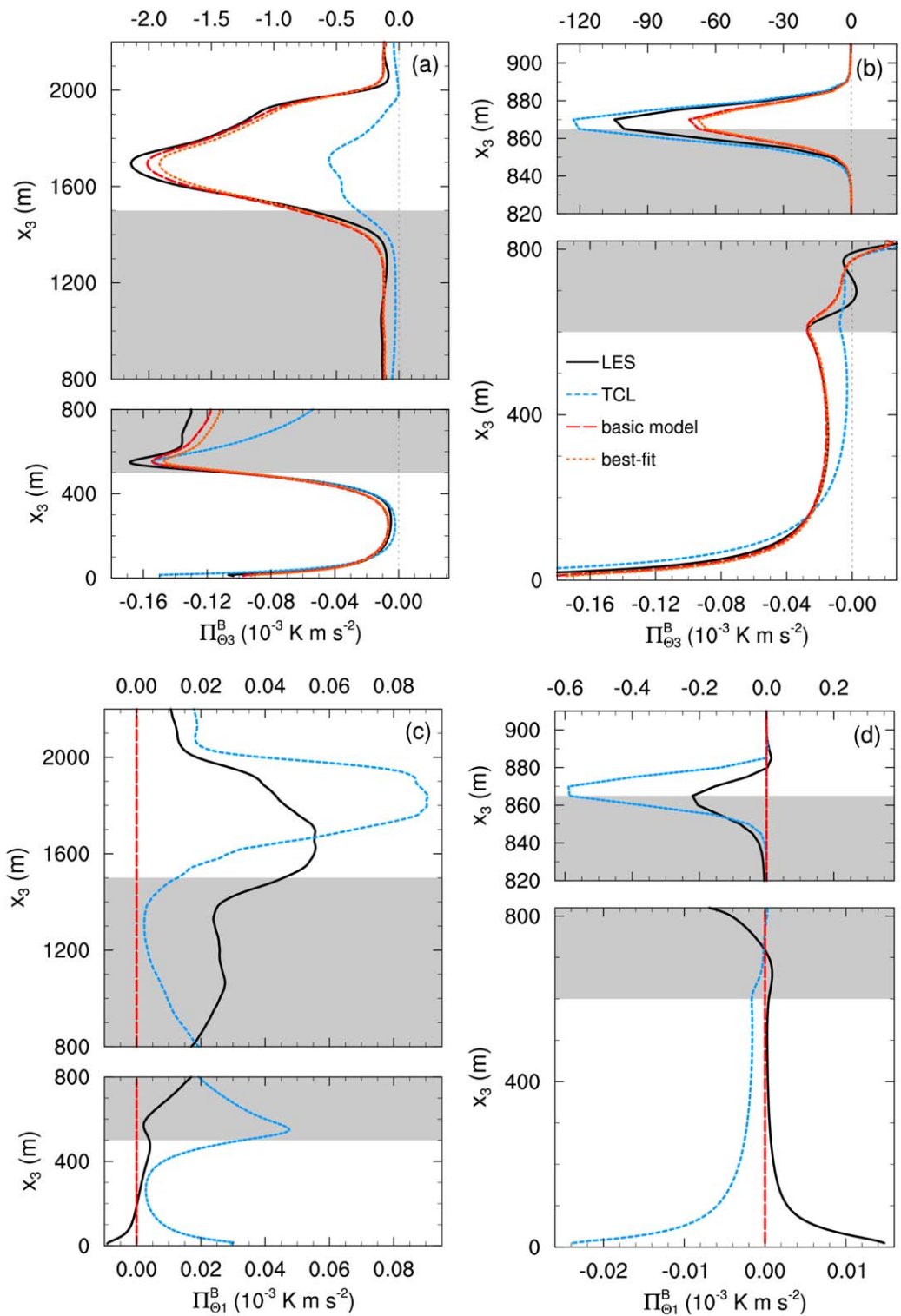
Figure 9. Vertical profiles of the buoyancy contribution to the vertical $\Pi_{\theta 3}^{B}$, (a) and (b), and horizontal $\Pi_{\theta 1}^{B}$, (c) and (d), components of the pressure gradient-liquid water potential temperature covariance. Solid black lines show $\Pi_{\theta 3}^{B}$ and $\Pi_{\theta 1}^{B}$ from LES data, short-dashed blue lines are based on the TCL model (25), and long-dashed red and dotted orange lines are based on the IP parameterization (23) of the basic model. The long-dashed red line is determined with $C_{B}^{s}=0.5$, and the dotted orange line, by means of the best-fit value for C_{B}^{s} which is 0.48 in Figure 9a, and 0.47 in Figure 9b (Table 4). A fitting in Figures 9c and 9d was not possible since (23) gives zero for these components. The BOMEX results are shown in Figures 9a and 9c, and the DYCOMS results are shown in Figures 9b and 9d. Ordinates are stretched at the top of the cloud layer. Different abscissa scales are used for the lower and upper part of the boundary layer in Figures 9a, 9b and 9d. Gray shading and time averaging as in Figure 1.

Table 4. Best-Fit Estimates of C_B^s [a]

	$\Pi_{\theta 1}^B$	$\Pi_{\theta 2}^B$	$\Pi_{\theta 3}^B$	$\Pi_{q 1}^B$	$\Pi_{q 2}^B$	$\Pi_{q 3}^B$	Lit.
C_B^s (B)	–	–	0.48 ± 0.08	–	–	0.51 ± 0.13	0.5
C_B^s (D)	–	–	0.47 ± 0.40	–	–	0.48 ± 0.19	0.5

[a]As in Table 1 but for the model constant C_B^s used in the IP parameterization (23). Literature values (Lit.) stem from *Moeng and Wyngaard* [1986]. Note that a fitting for the horizontal components of the pressure gradient-scalar covariances is not possible since (23) gives zero for these components.

Zeman [1981] proposed, based on *Launder et al.* [1975], another linear parameterizations for Π_{ij}^S and Π_{si}^S. They read

$$\Pi_{ij}^S = \left[\frac{4}{5} S_{ij} + C_{S1}^u \left(a_{ik} S_{jk} + a_{jk} S_{ik} - \frac{2}{3} \delta_{ij} a_{kl} S_{kl} \right) + C_{S2}^u \left(a_{ik} W_{jk} + a_{jk} W_{ik} \right) \right] E \tag{28}$$

and

$$\Pi_{si}^S = \left[C_{S1}^s S_{ij} + C_{S2}^s W_{ij} \right] \left(\left\langle \bar{u}_j'' \bar{s}'' \right\rangle + \left\langle \tau_{sj} \right\rangle \right), \tag{29}$$

where $C_{S1}^u = 12/7$, $C_{S2}^u = 0$, $C_{S1}^s = 3/5$ and $C_{S2}^s = 1$, and S_{ij} and W_{ij} are the symmetric and the antisymmetric parts of the mean-velocity gradient tensor:

$$\frac{\partial \langle \bar{u}_i \rangle}{\partial x_j} = \underbrace{\frac{1}{2} \left(\frac{\partial \langle \bar{u}_i \rangle}{\partial x_j} + \frac{\partial \langle \bar{u}_j \rangle}{\partial x_i} \right)}_{S_{ij}} + \underbrace{\frac{1}{2} \left(\frac{\partial \langle \bar{u}_i \rangle}{\partial x_j} - \frac{\partial \langle \bar{u}_j \rangle}{\partial x_i} \right)}_{W_{ij}}. \tag{30}$$

The values of model constants C_{S1}^u and C_{S2}^u are not independent as they are both functions of one more disposable parameter. That parameter can be determined by an additional constraint which *Zeman* [1981] based on rapid-distortion calculations [*Townsend*, 1970].

Zeman's parameterization (28) is equivalent to the IP parameterization (26) if $C_{S1}^u = C_{S2}^u = C_S^u = \frac{3}{5}$. Similarly for the pressure gradient-scalar covariance, if $C_{S1}^s = C_{S2}^s = C_S^s$, then equation (29) coincides with equation (27). Essentially this means that both linear parameterizations differ in the values of model constants only. Since *Zeman* [1981] uses $C_{S2}^s = 0$, the rotational part proportional to W_{ij} is neglected in (28).

In Figure 10, the shear contributions Π_{33}^S, Π_{12}^S, and Π_{13}^S computed from (26) and (28) are compared with the LES data. The value of $C_S^u = \frac{3}{5}$ is used in (26). Only *Zeman*'s parameterization is able to reproduce the diagonal element Π_{33}^S, at least qualitatively, near the surface in both CTBLs (Figures 10a and 10b). Close to the surface, the IP parameterization yields the shear contribution with the opposite sign as compared to LES. At the top of the mixed layer, $z \approx 500$ m for BOMEX and $z \approx 850$ m for DYCOMS, *Zeman*'s parameterization yields the opposite and the IP parameterization the same sign of Π_{33}^S as the LES. As the shear contribution Π_{33}^S is only significant close to the surface (see Figures 3c and 3d), the failure of a model for Π_{33}^S is tolerable at the subcloud layer top (but not close to the surface).

For the Π_{12}^S component (Figures 10c and 10d), both linear models agree well with the LES data. The best-fit estimates for C_S^u are 0.77 ± 0.78 for BOMEX and 0.80 ± 0.71 for DYCOMS (see Table 5). With due regard for the standard deviation, these estimates are close to the conventional value 0.6. Apart from the surface layer of both CTBLs and the entrainment layer of DYCOMS, the Π_{13}^S component is reproduced rather well by both linear models (Figures 10e and 10f). The best-fit estimates of C_S^u for the off-diagonal components of Π_{ij}^S are presented in Table 5. A fitting to the diagonal components is not performed. The fitting method used excludes the near-surface layer (see Appendix B for details). Then, the method is not able to give a true best-fit estimate because the IP parameterization gives a wrong sign of Π_{33}^S close to the surface (see, e.g., Figures 10a and 10b), i.e., where it really matters (well above the surface, Π_{33}^S is very small and the accuracy of its representation is not crucial). The best-fit estimates of C_S^u for the off-diagonal components of Π_{ij}^S are all smaller than one as the IP parameterization requires.

Figure 11 shows the horizontal component $\Pi_{\theta 1}^S$ of the shear contribution to the pressure gradient-liquid water potential temperature covariance. A comparison of $\Pi_{\theta 1}^S$ computed from (27) and (29) with the LES-based profiles reveals that both linear models are able to reproduce the shape of the $\Pi_{\theta 1}^S$ profile in both
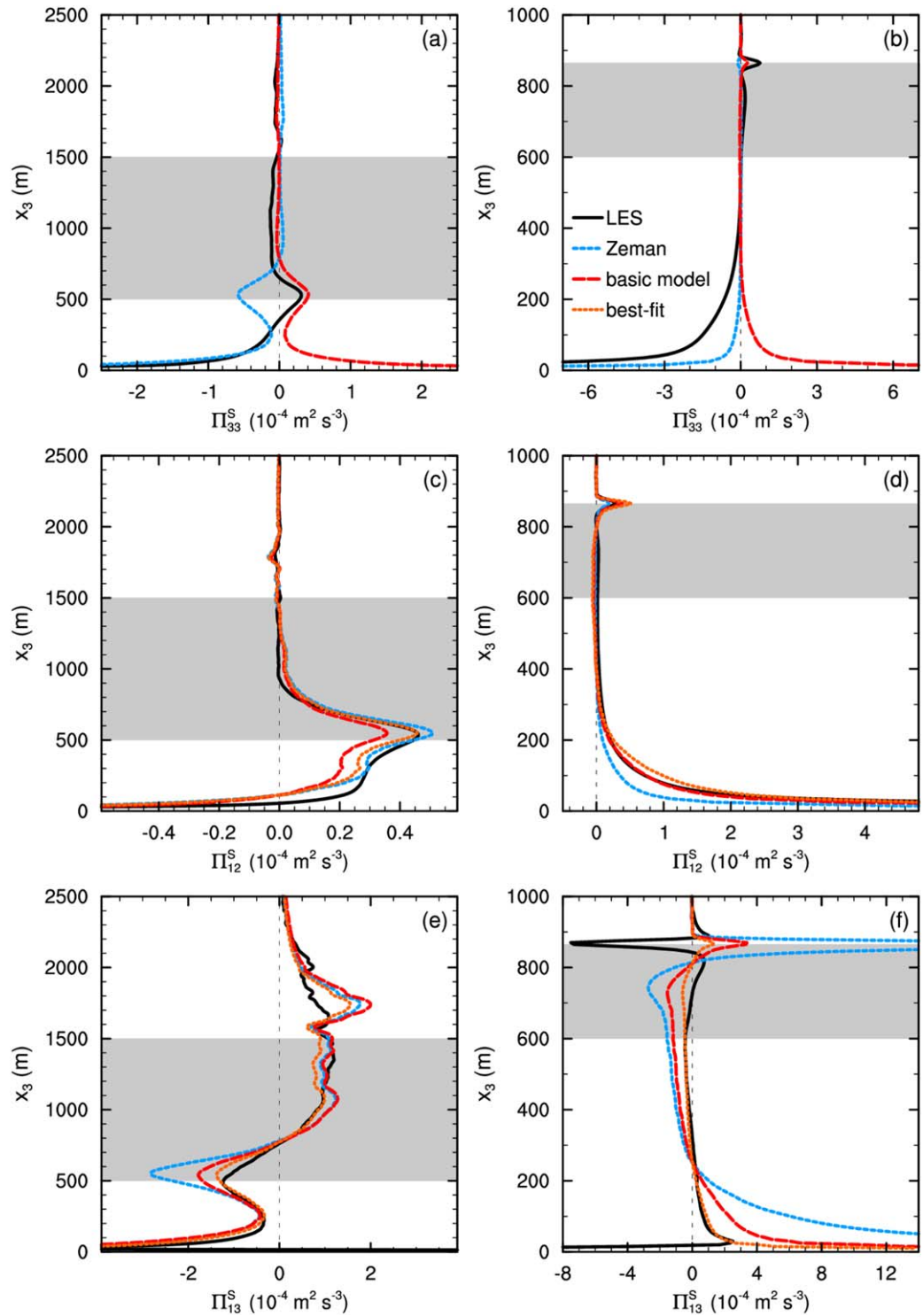
Figure 10. Vertical profiles of the mean-shear contribution to the pressure-strain covariance components Π_{33}^S, (a) and (b), Π_{12}^S, (c) and (d), and Π_{13}^S, (e) and (f). Solid black lines show Π_{33}^S, Π_{12}^S, and Π_{13}^S from LES data, short-dashed blue lines are based on the linear model (28) of *Zeman* [1981], and long-dashed red and dotted orange lines are based on the IP parameterization (26) of the basic model. The long-dashed red line is determined with $C_S^u = \frac{3}{5}$, and the dotted orange line, by means of the best-fit value for C_S^u which is 0.77 in Figure 10c, 0.80 in Figure 10d, 0.47 in Figure 10e, and 0.23 in Figure 10f (Table 5). No fitting is provided in Figures 10a and 10b. (See text for further details). The BOMEX results are shown in Figures 10a, 10c, and 10e, and the DYCOMS results are shown in Figures 10b, 10d, and 10f. Gray shading and time averaging as in Figure 1.

Table 5. Best-Fit Estimates of C_S^u [a]

	Π_{11}^S	Π_{22}^S	Π_{33}^S	Π_{12}^S	Π_{13}^S	Π_{23}^S	Lit.
C_S^u (B)	–	–	–	0.77 ± 0.78	0.47 ± 0.14	0.66 ± 0.69	$\frac{3}{5}$
C_S^u (D)	–	–	–	0.80 ± 0.71	0.23 ± 0.30	0.44 ± 0.61	$\frac{3}{5}$

[a]As in Table 1 but for the model constant C_S^u used in the IP parameterization (27). Note that a fitting for the diagonal components of Π_{ij}^S is not provided. (see section 3.4.3 for further details.) Literature values (Lit.) are taken from *Hanjalić and Launder* [2011, S. 68].

CTBLs. Near the stratocumulus top in DYCOMS and near the top of the subcloud layer in BOMEX, *Zeman*'s parameterization overestimates the LES data. The IP parameterization performs satisfactorily in the DYCOMS case. In the BOMEX case, the IP parameterization with $C_S^s = 0.5$ underestimates the LES data in the cumulus layer, and the use of the best-fit estimate of $C_S^s = 0.89$ results in an overestimation of the $\Pi_{\theta 1}^S$ maximum near the subcloud layer top. Table 6 contains the best-fit estimates of C_S^s for the horizontal components of the shear contribution to the pressure gradient-scalar covariance. All estimates of C_S^s are smaller than one (as required), but the range obtained on the basis of our LES is broader than the range $0.4 \leq C_S^s \leq 0.55$ given by *Hanjalić and Launder* [2011, p. 68].

For the vertical component of Π_{si}^S, the IP parameterization (27) yields zero due to zero mean vertical velocity. *Zeman*'s parameterization (29) is able to give an order of magnitude estimate of Π_{s3} but fails to reproduce the shape of the LES-based profiles (not shown). As the shear contribution Π_{s3} is of minor importance in comparison to the buoyancy and turbulence-turbulence contributions (see Figure 5), a very accurate representation of Π_{s3}^S is not crucial for modeling the total pressure gradient-scalar covariance.
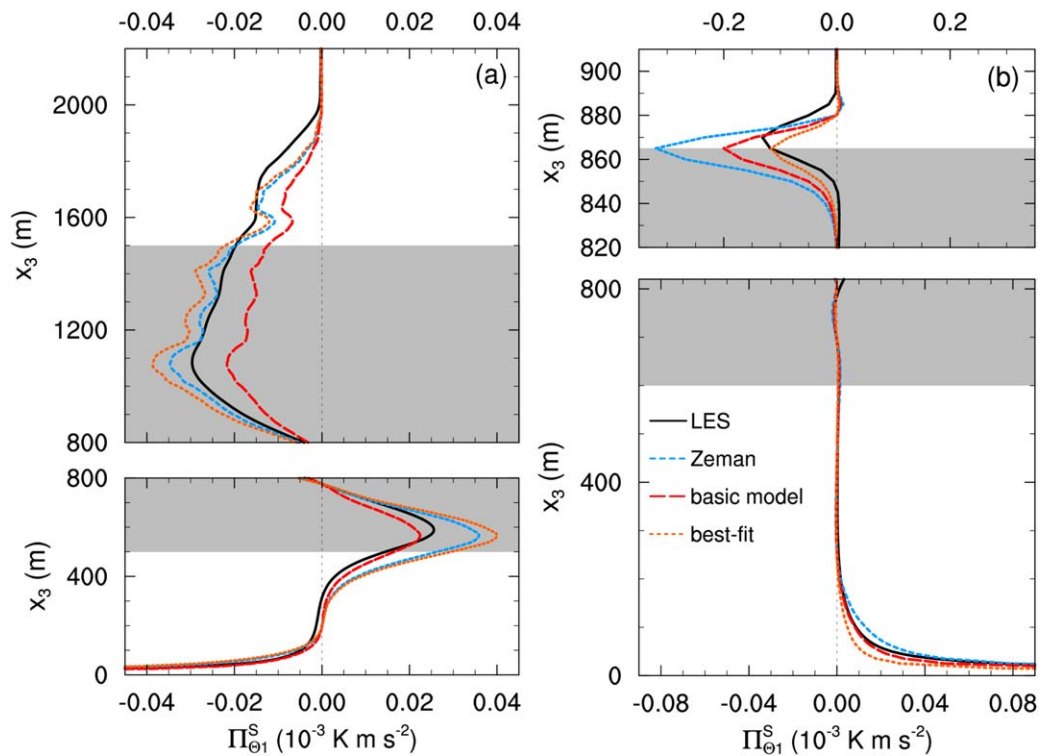
Figure 11. Vertical profiles of the shear contribution to the horizontal component $\Pi_{\theta 1}^S$ of the pressure gradient-liquid water potential temperature covariance for BOMEX (a) and DYCOMS (b). Solid black lines show $\Pi_{\theta 1}^S$ from LES data, short-dashed blue lines are based on the linear model (25) of *Zeman* [1981], and long-dashed red and dotted orange lines are based on the IP parameterization (27) of the basic model. The long-dashed red line is determined with $C_S^s = 0.5$, and the dotted orange line, by means of the best-fit value for C_S^s which is 0.89 in Figure 11a, and 0.29 in Figure 11b (Table 6). Ordinates are stretched at the top of the cloud layer. Different abscissa scales are used for the lower and upper part of the boundary layer in Figure 11b. Gray shading and time averaging as in Figure 1.

Table 6. Best-Fit Estimates of C_S^s [a]

	$\Pi_{\theta 1}^S$	$\Pi_{\theta 2}^S$	$\Pi_{\theta 3}^S$	Π_{q1}^S	Π_{q2}^S	Π_{q3}^S	Lit.
C_S^s (B)	0.89 ± 0.96	0.78 ± 0.93	–	0.91 ± 0.72	0.77 ± 0.94	–	0.4–0.55
C_S^s (D)	0.29 ± 0.98	0.70 ± 1.28	–	0.46 ± 0.19	0.45 ± 0.96	–	0.4–0.55

[a]As in Table 1 but for the model constant C_S^s used in the IP parameterization (27). Literature values (Lit.) are taken from *Hanjalić and Launder* [2011, S. 68]. Note that a fitting for the vertical pressure gradient-scalar covariances is not possible due to zero horizontal-mean vertical velocity.

4. Conclusions

High-resolution large-eddy simulations are used to perform a detailed analysis of the pressure-scrambling terms, i.e., the pressure-strain and the pressure gradient-scalar covariances in the Reynolds-stress and scalar-flux budgets, respectively, in the cumulus-topped (BOMEX) and stratocumulus-topped (DYCOMS-II, RF01) boundary-layer flows. Recall that the pressure-strain covariance in the Reynolds-stress budget acts to redistribute the turbulence energy evenly between its components and thereby drives turbulence towards an isotropic state. The pressure gradient-scalar covariance in the scalar-flux budget also drives turbulence toward an isotropic state by reducing the magnitude of the scalar flux and the difference between the flux components. Using LES, the pressure-scrambling terms are decomposed into contributions due to turbulence-turbulence interactions, buoyancy, mean velocity shear, and Coriolis effects. The performance of some commonly used parameterizations for the aforementioned contributions to the pressure-scrambling terms is tested against LES data.

The decomposition of the pressure-strain covariance Π_{ij} shows that the contributions due to turbulence-turbulence interactions Π_{ij}^T and buoyancy Π_{ij}^B are the most important ones in cloud-topped boundary layers. The Coriolis contribution Π_{ij}^C is negligibly small. The mean velocity shear contribution Π_{ij}^S is important near the surface, but it is of minor importance inside the cloud layers (where it can safely be neglected, at least in the CTBL regimes considered in the present study). The buoyancy and the turbulence-turbulence contributions are of the same order of magnitude in the cumulus cloud layer. In the stratocumulus cloud layer, the buoyancy contribution dominates. The analysis of Π_{ij} shows that the turbulence-turbulence contribution and the total pressure-strain covariance may have opposite sign in some parts of the flow. This is the case for e.g., Π_{11} and Π_{33} near the surface and in the upper part of the cloud layer in the stratocumulus-topped boundary layer. Then, applying Rotta return-to-isotropy parameterization to the entire pressure-scrambling term (and not to the slow return-to-isotropy part only) in the Reynolds-stress budget may cause the model failure, since even the sign of Π_{ij} may not be obtained correctly.

The pressure gradient-liquid water potential temperature covariance $\Pi_{\theta i}$ and the pressure gradient-total water specific humidity covariance Π_{qi} are similar in terms of the relative importance of the various contributions and (with some reservations) in terms of shapes of their vertical profiles. The vertical component of the pressure gradient-scalar covariance Π_{s3} (s stands for either θ_l or q_t) is dominated by the buoyancy in the inversion layer. In the remainder of the boundary layer in both cases, the turbulence-turbulence and the buoyancy contributions are roughly equally important. The shear contribution to Π_{s3} is small even close to the surface. The horizontal component of pressure gradient-scalar covariances are roughly equally composed of buoyancy, shear, and turbulence-turbulence contributions in the subcloud and the cloud layers, while the shear contribution dominates close to the surface.

The pressure-scrambling terms estimated on the basis of LES data are used to test the applicability of two different models for the turbulence-turbulence, buoyancy, and shear contributions to the pressure-scrambling terms to the boundary layers capped by shallow clouds. The two models are a simple "basic model" (including the Rotta-type parameterization for the slow turbulence-turbulence contributions and the parameterizations for the rapid buoyancy and shear contributions that are linear in the second-order moments involved) and a more complex two-component-limit (TCL) model (nonlinear in the second-order moments). For the basic model, the "conventional" values of the model constants taken from literature are used along with the "best-fit" values that are determined by means of a least-square method (see Appendix B).

Consideration of the turbulence-turbulence contribution to the pressure-strain covariance shows that both the Rotta-type relaxation parameterization of the basic model and the TCL parameterization are able to reproduce the principal features of the LES-based profiles with approximately the same accuracy. This

Table 7. Performance of the Tested Models With Respect to the Various Contributions to Pressure-Strain and Pressure Gradient–Scalar Covariances

	Π_{ij}^T	Π_{si}^T	Π_{ij}^B	Π_{si}^B	Π_{ij}^S	Π_{si}^S
bm-IP	G	G	diag. comp.: A Off-diag. comp.: G	vert. comp.: G hor. comp.: F	G (but Π_{33}^S: F)	G
bm-Z	−	−	−	−	G	G
TCL	G	G	diag. comp.: A Off-diag. comp.: G	vert. comp.: G hor. comp.: A	−	−

ᵃThe abbreviation bm-IP denotes the basic model (bm) where the IP parameterization for the buoyancy and the shear contributions is used. bm-Z is the basic model where the parameterization of *Zeman* [1981] is used for the shear contributions. See text for further explanation of the ratings G (good), A (acceptable), F (fail).

conclusion is also valid for the pressure gradient-scalar covariances (except for the region near the cloud top in both CTBLs, where both parameterizations reveal large deviations from the LES data). Thus, using a more complex TCL model instead of a rather simple Rotta-type parameterization does not result in a better agreement with LES data in the regimes considered in the present study.

Both the linear isotropization-of-production parameterization of the basic model and the nonlinear TCL parameterization do a reasonable job in describing the diagonal components of the buoyancy contribution to the pressure-strain covariance. However, both parameterizations fail to describe the peaks of Π_{11}^B and Π_{33}^B at the top of the stratocumulus layer and the nonlinear shape of the Π_{11}^B and Π_{33}^B profiles in the sub-cloud layer of both CTBLs. The off-diagonal component Π_{13}^B of the buoyancy contribution to the pressure-strain covariance is reproduced quite satisfactorily with both parameterizations.

A simple linear parameterization of the vertical component of the buoyancy contribution to the pressure gradient-scalar covariance shows a good performance in both CTBLs. It gives somewhat better agreement with the LES data than the more sophisticated TCL parameterization. However, the horizontal components of the buoyancy contribution to the pressure gradient-scalar covariance cannot be correctly reproduced by a linear parameterization. The oversimplified linear model yields horizontal components that are identically zero. The TCL model is able to give an order-of-magnitude estimate of the horizontal components, but the shape of the profiles cannot be reproduced satisfactorily.

Two parameterizations of the mean velocity shear contributions to the pressure-scrambling terms are tested against the LES data, namely, the IP parameterization and the parameterization of *Zeman* [1981] (the TCL parameterizations for the shear contributions are not tested). These parameterizations are, in fact, very similar. They are both linear in the second-moments but they differ in the values of their dimensionless con-stants. Both the IP parameterization and the *Zeman* parameterization appear to be capable of describing most components of the pressure-scrambling terms reasonably well. The exceptions are the diagonal com-ponents of the pressure-strain covariance (exemplified by Π_{33}^S), for which the IP parameterization fails as even the sign of the components in question cannot be given correctly.

Table 7 provides a summary of performance of parameterizations (models) of the pressure-scrambling terms in the atmospheric boundary layers capped by shallow clouds. A model is rated as good (**G**) if the shape of the LES-based vertical profile of the contribution in question is reproduced satisfactorily in most parts of the CTBL. A model is rated as acceptable (**A**) if the sign of the contribution is reproduced correctly (at least in most parts of the CTBL) but the LES-based and the modeled vertical profiles are largely dissimilar in terms of their shapes. A model fails (**F**) if even the sign of the contribution is not reproduced correctly. A dash "−" in Table 7 indicates that a model of the respective contribution is not tested (e.g., the TCL model for the shear contributions).

Finally, the implications of results from the present study for modeling (parameterizing) turbulence in the atmosphere should be briefly discussed. As the above analysis suggests, simple linear parameterizations of the pressure-scrambling terms in the Reynolds-stress and scalar-flux budgets do not appear to be inferior to more complex TCL parameterizations in the boundary-layer regimes considered. Linear parameterizations fail to describe some contributions to the pressure-scrambling terms but are able to describe the principal features of most contributions reasonably well. It is the opinion of the present authors, however, that the TCL parameterizations (or similar nonlinear realizable parameterizations) should still be given preference

over simple linear parameterizations when modeling turbulence in the atmosphere. The point is that a turbulence parameterization scheme used within a numerical model of atmospheric circulation should deal with many very different turbulence regimes encountered in the Earth's atmosphere, not with some particular regimes only. Although the TCL and the simplified linear parameterizations are found to perform similarly in the particular CTBL regimes considered in the present study, the TCL and similar parameterizations are more flexible and have the potential to realistically describe various turbulence regimes. Simplified linear parameterizations are less flexible; they can describe some particular turbulence regimes but will almost inevitably fail in the other regimes for which they have not been tuned. As an illustrative example, consider the nonlinear TCL parameterization, equation (25), and the linear parameterization, equation (23), for the buoyancy contribution to the pressure gradient-scalar covariance. Equation (25) is valid in both the isotropic limit and in the two-component limit, where the latter constraint is vitally important to model turbulence in stable density stratification. The linear parameterization (23) with $C_B^s = 0.5$ appears to describe the vertical component of the buoyancy contribution to the pressure gradient-scalar covariance better than the TCL parameterization (25). However, the linear parameterization entirely fails in describing the horizontal components of the buoyancy contribution to the pressure gradient-scalar covariance. Furthermore, (23) with $C_B^s = 0.5$ will also fail in the two-component limit, where C_B^s should be equal to 1 in order to avoid spurious generation of the scalar fluxes by the buoyancy forces. Setting $C_B^s = 1$ satisfies the two-component limit and helps describing turbulence in strongly stratified flows (regions of the flow), but then the linear parameterization will fail in the isotropic limit and in convective flows, where the buoyancy production of turbulence will be strongly underestimated. That is, the linear model is not able to satisfy a number of important constraints simultaneously, simply by construction. We, therefore, tend to think that the research efforts should go into further development of flexible and physically plausible nonlinear parameterizations of the pressure-scrambling terms and (which is important for applications) into their optimization in terms of computational efficiency.

Although nonlinear, intrinsically realizable parameterizations of the pressure-scrambling terms are more attractive than linear parameterizations, it seems unlikely that they will be widely used in practical applications in the short-term to medium-term prospects. Simplified linear parameterizations will most likely be utilized in numerical weather prediction, climate modeling, and related applications for some, perhaps many, years to come. Then a modeler has to face a very difficult "tuning dilemma." Tuning the model constants (such as C_B^s) to describe particular flow regimes in the best possible way, one should put up with possible large uncertainties in the other regimes. An accurate description of many turbulence regimes is not possible due to inflexibility of linear parameterizations (which have too few degrees of freedom to satisfy several important constraints). The following pragmatic way out can be suggested to avoid big trouble. A turbulence parameterization scheme utilizes simplified parameterizations of the pressure-scrambling terms, including the Rotta-type parameterizations for the slow turbulence-turbulence contributions and the (linear in second-moments) parameterizations for the rapid buoyancy, shear, and Coriolis contributions. However, the model constants are replaced with empirically-based functions of the dimensionless governing parameters (such as, e.g., the gradient Richardson number) constructed so that to satisfy the necessary constraints. In this way, the resulting parameterizations remain rather simple and computationally inexpensive, but large errors caused by the shortcomings of the linear parameterizations of the pressure-scrambling terms can be avoided. A model of the stably stratified atmospheric boundary layer, that avoids spurious generation of the heat flux through the use of a function of the gradient Richardson number instead of a constant value of C_B^s in the linear parameterization (23), was proposed by *Wyngaard* [1975].

As the two CTBLs considered in the present study are dominated by buoyancy, less attention is paid to the shear contributions to the pressure-scrambling terms than to the turbulence-turbulence and buoyancy contributions. Consideration of convective flows, where the role of mean velocity shear is large (or even dominant), is beyond the scope of the present study. A detailed analysis of the pressure-scrambling terms in such flows, including the evaluation of complex, nonlinear parameterizations (such as the TCL parameterization), is of considerable interest and should be performed in the future using LES (or DNS).

Appendix A: Determination of Fluctuating Pressure Components in PALM

The decomposition of the fluctuating pressure, equation (5), is linear. Thus, the total fluctuating pressure $\bar{p}''$ should be numerically equal to the sum of its components. To ensure this equality, we took care that the

Poisson equations for the pressure components are solved in the same way as the Poisson equation for the total pressure $\bar{p}$ in the LES model PALM. This online approach, where the pressure components are determined during the LES model run, guarantees that precisely the same numerics are applied to the pressure components and to the total pressure.

In the incompressible LES model PALM, a predictor-corrector method (also called fractional-step or projection method [e.g., *Chorin*, 1968, 1969; *Patrinos and Kistler*, 1976]) is used to calculate a flow free of divergence. This method splits the integration of the model equations into two steps. In the first predictor step, the momentum equations are solved without the pressure-gradient term yielding a preliminary velocity field which is generally not free of divergence. The divergence of the preliminary velocity field is then used as a source term in the Poisson equation for pressure. Once the pressure equation is solved, the preliminary velocity field is corrected by means of the pressure-gradient term in the second corrector step. Overall, this method guarantees the calculation of an incompressible flow.

The individual pressure components are determined in the same manner as the total pressure. First, the tendencies of the LES momentum equations due to advection (A), buoyancy (B), Coriolis effect (C), subgrid diffusion (SG), and large-scale subsidence (SU) are stored separately. In the predictor step, provisional velocity fields based on each process are calculated. In the corrector step, the divergences of the provisional velocity fields are determined which are then, in turn, the source terms of the respective Poisson equations. These equations are solved in the LES model by means of fast Fourier transforms, and the pressure components are obtained.

A comment on the boundary conditions for the pressure components should be made. At the surface, a zero-gradient condition is used for each component. This is not fully consistent with the momentum equations as described in section 2.2, since the buoyancy gradient and the divergence of the subgrid scale stress are generally nonzero at the surface. However, with regard to the fact that the predictor-corrector method is used to determine the pressure components, a pressure boundary condition is not required at the surface. The reason is that by using the predictor-corrector method on a staggered grid formulated in discrete space, a definition of a pressure boundary condition at the wall is not needed [e.g., *Vreman*, 2014]. Thus, we argue that, despite the somewhat inconsistent choice of the pressure boundary conditions, physically meaningful results are obtained.

At the top of the model domain, a zero pressure (Dirichlet) boundary condition is assumed for all components. This is somewhat inconsistent with regard to the top boundary conditions discussed in section 2.2. However, concerning the pressure boundary condition at the model top, zero-gradient (Neumann) and zero pressure (Dirichlet) conditions are roughly equivalent if there are vanishing velocity and scalar fluctuations at the model top. This is the case in our simulations since Rayleigh damping is used toward the model top. Sensitivity tests with a zero-gradient condition at model top (results are not shown) indicate that the pressure components and the turbulence statistics are very little affected by the type of the pressure boundary condition applied at the top of the computational domain.

The method described above provides the pressure components $\bar{p}_A$ due to advection, $\bar{p}_B$ due to buoyancy, $\bar{p}_C$ due to Coriolis effect, $\bar{p}_{SG}$ due to subgrid diffusion, and $\bar{p}_{SU}$ due to large-scale subsidence.

To separate the contributions due to turbulence-turbulence interactions (T) and mean shear (S), we consider the source term of the Poisson equation for the pressure component due to advection:

$$
\frac{1}{\rho_0}\frac{\partial^2 \bar{p}_A}{\partial x_i^2} = -\frac{\partial^2 \left(\bar{u}_i \bar{u}_j\right)}{\partial x_i \partial x_j}
$$
$$
= -\frac{\partial^2 \bar{u}_i'' \bar{u}_j''}{\partial x_i \partial x_j} - 2\frac{\partial \bar{u}_j''}{\partial x_i}\frac{\partial \langle \bar{u}_i \rangle}{\partial x_j}.
$$

(A1)

The first term on the right-hand-side of (A1) is equivalent to the source term of the pressure contribution due to turbulence-turbulence interactions in equation (6) and the second term is equivalent to the source term for the mean-shear pressure contribution in equation (7). This implies that

$$
\bar{p}_A = \bar{p}_T + \bar{p}_S.
$$

(A2)

The contribution due to advection, $\bar{p}_A$, is determined by solving (A1). The shear contribution $\bar{p}_S$ is calculated by solving (7) in the LES model where its source term is determined based on the velocity fields at the

current time step. The turbulence-turbulence contribution is then determined by means of (A2) as a difference $\bar{p}_T = \bar{p}_A - \bar{p}_S$.

It should be noted that our LES model solves for a modified pressure which is the sum of the pressure and the trace of the subgrid scale stress. This trace is subtracted from the subgrid scale part of the pressure.

Appendix B: Determination of Best-Fit Values for Model Constants

All parameterizations of the basic model (see equations (18), (19), (23), (23), (27), and (27)) are essentially a product of a model constant C and a function $f(x_3)$. This product is fitted to the LES profiles of the pressure-scrambling terms denoted as $\Pi_{LES}(x_3)$. The following model is used to evaluate C: $\Pi_{LES}(x_3) = C \cdot f(x_3)$. By means of linear regression the model constant C can now be calculated with $C = [\Pi_{LES}(x_3)/f(x_3)]_{x_3}$ where $[\cdots]_{x_3}$ denotes a mean over vertical levels. Thus, the best-fit constant is just the vertical mean of the ratio of LES-based pressure covariance and $f(x_3)$. The root-mean-square error (RMSE) is also provided. The fitting is applied over the middle part of the boundary layer, at $100\,m < z < 2000\,m$ for BOMEX and at $100\,m < z < 800\,m$ for DYCOMS, excluding the near-surface layer and the interfacial layer. Close to the surface, the LES fields are chiefly determined by the subgrid model and are less reliable. The interfacial layer is excluded from the fitting since the strong gradients in the stratocumulus case are not well resolved. Furthermore, a weighting is applied in the course of the vertical averaging to soften the influence of outliers on the mean. Only those values of $\Pi_{LES}(x_3)/f(x_3)$ are used to compute the vertical mean that are within a certain range around the literature value c_{lit} of the particular model constant. This range was chosen arbitrarily to $c_{lit} \pm 5$. Using ranges between 2 and 7 has only minor impact on the resulting best-fit values.

References

Andrén, A., and C.-H. Moeng (1993), Single-point closure in a neutrally stratified boundary layer, *J. Atmos. Sci.*, *50*, 3366–3379, doi:10.1175/1520-0469(1993)050 < 3366:SPCIAN>2.0.CO;2.

Chorin, A. J. (1968), Numerical solution of the Navier-Stokes equations, *Math. Comput.*, *22*, 745–762, doi:10.1090/S0025-5718-1968-0242392-2.

Chorin, A. J. (1969), On the convergence of discrete approximations to the Navier-Stokes equations, *Math. Comput.*, *23*, 341–343, doi:10.1090/S0025-5718-1969-0242393-5.

Craft, T. J., N. Z. Ince, and B. E. Launder (1996), Recent developments in second-moment closure for buoyancy affected flows, *Dyn. Atmos. Oceans*, *23*, 99–114, doi:10.1016/0377-0265(95)00424-6.

Groth, J. (1991), Description of the pressure effects in the Reynolds stress transport equations, *Phys. Fluids A*, *3(9)*, 2276–2277, doi:10.1063/1.857908.

Hadfield, M. G., W. R. Cotton, and R. A. Pielke (1988), Comments on "An analysis of closures for the pressure-scalar covariances in the convective boundary layer", *J. Atmos. Sci.*, *45*, 1970–1972, doi:10.1175/1520-0469(1988)045 <1970:COAOCF>2.0.CO;2.

Hanjalić, K., and B. Launder (2011), *Modelling Turbulence in Engineering and the Environment: Second-Moment Routes to Closures*, 379 pp., Cambridge Univ. Press, Cambridge, U.K.

Heinze, R., D. Mironov, and S. Raasch (2015), Second-moment budgets in cloud-topped boundary layers: A large-eddy simulation study, *J. Adv. Model. Earth Syst.*, *7*, 510–536, doi:10.1002/2014MS000376.

Launder, B. E., G. J. Reese, and W. Rodi (1975), Progress in the development of a Reynolds-stress turbulence closure, *J. Fluid Mech.*, *68*, 537–566, doi:10.1017/S0022112075001814.

Lenschow, D. H., J. C. Wyngaard, and W. T. Pennel (1980), Mean-field and second-moment budgets in a baroclinic, convective boundary layer, *J. Atmos. Sci.*, *37*, 1313–1326, doi:10.1175/1520-0469(1980)037 <1313:MFASMB>2.0.CO;2.

Lumley, J. L. (1975), Pressure-strain correlation, *Phys. Fluids.*, *18*, 750, doi:10.1063/1.861205.

Lumley, J. L. (1978), Computational modeling of turbulent flows, *Adv. Appl. Mech.*, *18*, 123–176.

Maronga, B., M. Gryschka, R. Heinze, F. Hoffmann, F. Kanani-Sühring, M. Keck, K. Ketelsen, M.-O. Letzel, M. Sühring, and S. Raasch (2015), The Parallelized Large-Eddy Simulation Model (PALM) version 4.0 for atmospheric and oceanic flows: Model formulation, recent developments, and future perspectives, *Geosci. Model Dev. Discuss.*, *8*(2), 1539–1637, doi:10.5194/gmdd-8-1539-2015.

Miles, N. L., J. C. Wyngaard, and M. J. Otte (2004), Turbulent pressure statistics in the atmospheric boundary layer from large-eddy simulation, *Boundary Layer Meteorol.*, *113*, 161–185, doi:10.1023/B:BOUN.0000039377.36809.

Mironov, D. V. (2001), Pressure-potential temperature covariance in convection with rotation, *Q. J. R. Meteorol. Soc.*, *127*, 89–110, doi:10.1256/smsqj.57105.

Mironov, D. V. (2009), Turbulence in the lower troposphere: Second-order closure and mass-flux modelling frameworks, in *Interdisciplinary Aspects of Turbulence, Springer Lecture Notes in Physics*, vol. 756, edited by W. Hillebrandt and F. Kupka, Springer, Berlin, doi:10.1007/978-3-540-78961-1_5.

Mironov, D. V., V. M. Gryanik, C.-H. Moeng, D. J. Olbers, and T. H. Warncke (2000), Vertical turbulence structure and second-moment budgets in convection with rotation: A large-eddy simulation study, *Q. J. R. Meteorol. Soc.*, *126*, 477–515, doi:10.1256/smsqj.56305.

Moeng, C.-H., and J. C. Wyngaard (1986), An analysis of closures for pressure-scalar convariances in the convective boundary layer, *J. Atmos. Sci.*, *43*, 2499–2513.

Monin, A. S. (1965), On the symmetry of turbulence in the surface layer of air, *Atmos. Oceanic Phys. Engl. Transl.*, *1*(1), 25–30.

Naot, D., A. Shavit, and M. Wolfshtein (1970), Interactions between components and the redistribution of Reynolds stress, *Isr. J. Technol.*, *8*, 259–269.

Nguyen, K. X., T. W. Horst, S. P. Oncley, and C. Tong (2013), Measurements of the budgets of the subgrid-scale stress and temperature flux in a convective atmospheric surface layer, *J. Fluid Mech.*, *729*, 388–422, doi:10.1017/jfm.2013.302.

Nishiyama, R. T., and A. J. Bedard (1991), A "Quad-Disc" static pressure probe for measurement in adverse atmospheres: With a comparative review of static pressure probe designs, *Rev. Sci. Instrum.*, *62*, 2193–2204, doi:10.1063/1.1142337.

Patrinos, A. A. N., and A. L. Kistler (1976), A numerical study of the Chicago lake breeze, *Boundary Layer Meteorol.*, *12*, 92–123, doi:10.1007/BF00116400.

Pope, S. B. (2000), *Turbulent Flows*, 771 pp., Cambridge Univ. Press, Cambridge, U. K.

Raasch, S., and M. Schröter (2001), PALM – A large-eddy simulation model performing on massively parallel computers, *Meteorol. Z.*, *10*, 363–372, doi:10.1127/0941-2948/2001/0010-0363.

Ristorcelli, J. R., J. L. Lumley, and R. Abid (1995), A rapid-pressure covariance representation consistent with the Taylor-Proudman theorem materially frame indifferent in the two-dimensional limit, *J. Fluid Mech.*, *292*, 111–152, doi:10.1017/S0022112095001467.

Rotta, J. C. (1951), Statistische Theorie nichthomogener Turbulenz. 1., *Z. Phys.*, *129*, 547–572, doi:10.1007/BF01330059.

Siebesma, A. P., et al. (2003), A large eddy simulation intercomparison study of shallow cumulus convection, *J. Atmos. Sci.*, *60*, 1201–1219, doi:10.1175/1520-0469(2003)60 <1201:ALESIS>2.0.CO;2.

Speziale, C. G. (1985), Modeling the pressure gradient-velocity correlation of turbulence, *Phys. Fluids*, *28*, 69–71, doi:10.1063/1.865127.

Stevens, B., et al. (2005), Evaluation of large-eddy simulations via observations of nocturnal marine stratocumulus, *Mon. Weather Rev.*, *133*, 1443–1462, doi:10.1175/MWR2930.1.

Stull, R. B. (1988), *An Introduction to Boundary Layer Meteorology*, 666 pp., Kluwer Acad., Springer, Netherlands.

Townsend, A. (1970), Entrainment and the structure of turbulent flow, *J. Fluid Mech.*, *41*, 13–46, doi:10.1017/S0022112070000514.

Umlauf, L., and H. Burchard (2005), Second-order turbulence closure models for geophysical boundary layers. a review of recent work, *Cont. Shelf Res.*, *25*, 795–827, doi:10.1016/j.csr.2004.08.004.

Vreman, A. W. (2014), The projection method for the incompressible Navier Stokes equations: The pressure near a no-slip wall, *J. Comput. Phys.*, *263*, 353–374, doi:10.1016/j.jcp.2014.01.035.

Wilczak, J. M. (1984), Large-scale eddies in the unstably stratified atmospheric surface layer. Part I: Velocity and temperature structure, *J. Atmos. Sci.*, *41*, 3537–3550, doi:10.1175/1520-0469(1984)04 < 3537:LSEITU>2.0.CO;2.

Wilczak, J. M., and A. J. Bedard (2004), A new turbulence microbarometer and its evaluation using the budget of horizontal heat flux, *J. Atmos. Oceanic Technol.*, *21*, 1170–1181, doi:10.1175/1520-0426(2004)021 < 1170:ANTMAI>2.0.CO;2.

Wyngaard, J. C. (1975), Modeling the planetary boundary layer: Extension to the stable case, *Boundary Layer Meteorol.*, *9*, 441–460, doi: 0.1007/BF00223393.

Wyngaard, J. C., and O. R. Coté (1971), The budgets of the turbulent kinetic energy and temperature variance in the atmospheric surface layer, *J. Atmos. Sci.*, *28*, 190–201, doi:10.1175/1520-0469(1971)028 < 0190:TBOTKE>2.0.CO;2.

Zeman, O. (1981), Progress in the modelling of planetary boundary layers, *Annu. Rev. Fluid Mech.*, *13*, 253–272, doi:10.1146/annurev.fl.13.010181.001345.